03,09

Generation of terahertz radiation in semiconductors (Review)

© A.V. Andrianov

Ioffe Institute,
St. Petersburg, Russia
E-mail: alex.andrianov@mail.ioffe.ru

Received July 7, 2023
Revised September 1, 2023
Accepted September 3, 2023

Electromagnetic radiation in the terahertz frequency range, occupying the spectral region between optical infrared and microwave radiation, is of interest for numerous diagnostic applications in various fields of science and technology. To build terahertz diagnostic systems, various types of radiation sources are required. This review considers schemes for the generation of terahertz radiation in semiconductors and semiconductor structures based both on quantum optical transitions between different energy levels in the system and generation schemes not directly related to quantum transitions, which can be attributed to classical schemes.

Keywords: Optical transitions, lasers, light-emitting diodes, ultrashort optical pulses, fast dipole moment, fast photocurrent.

DOI: 10.61011/PSS.2023.10.57208.142

Table of Content

1. Introduction

It is generally accepted that the terahertz (THz) range of the spectrum of electromagnetic waves lies in the frequency range of 0.1 to 10 THz (at wavelengths of 3 mm to 30 μm) [1], although a number of authors shift the upper frequency of this range to 15–20 THz, which reflects some blurring of the boundaries of THz range [2]. Electromagnetic THz emission occupies the region of the spectrum between infrared (IR) light and microwave radiation, and is also called far-infrared radiation. This range is unique in that just in the THz region the main characteristic spectral features of various compounds, environments and biological tissues, molecular oscillations and atomic transitions in Rydberg states fall. Besides, the THz region includes resonance frequencies associated with transitions between the states of shallow impurity centers and excitons in semiconductors, as well as frequencies of transitions between levels of size quantization of electrons

and holes in low-dimensional structures. Significant interest in the far-IR or THz range, in spectroscopy in this range, appeared after the end of World War II and was caused by occurred problems in astronomy and chemistry related to the spectroscopy of vibrational and rotational transitions in various molecules [3]. At that time, the THz tools were extremely limited, mainly due to the lack of compact, fast, reliable, and at the same time intense radiation sources and sensitive receivers. Over the past 30−35 years enormous progress has been made in the development of THz-band tools. Semiconductor THz quantum-cascade lasers appeared, a new technique of THz spectroscopy was formed — THz time-domain spectroscopy (THz-TDS), based on generation and detection of broadband pulsed THz emission using pulses from femtosecond lasers in the visible or near-IR ranges, as well as fast Fourier transform of THz waveforms [1–4]. The successes achieved in the creation of THz-range devices and the development of THz technologies are largely related to successes in the study of non-equilibrium phenomena in solids and, in particular, in semiconductors.

This review will consider the generation of THz emission in semiconductors and semiconductor structures using both quantum transitions between electronic energy levels and classical methods for generating THz emission, based, in particular, on excitation by femtosecond laser pulses of fast dipole moment or short burst of photocurrent, which form the basis of the THz-TDS technique. Issues of detecting THz emission are also very important for the THz technologies development, and semiconductor structures play a significant role here. The principles and approaches to detecting THz emission using semiconductor structures are presented in a number of reviews (see, for example, reviews [3–5], as well as new reviews [6,7]), and therefore will not be considered here.

2. THz emission during quantum optical transitions in semiconductors

2.1. Quantum cascade structures

2.1.1. Background

The invention of the quantum cascade laser (QCL), initially demonstrated for wavelengths in the mid-IR range, and 8 years later resulted in the creation of laser for THz range [9], essentially opened a new era in semiconductor optoelectronics. The QCL structure is a multi-period system of tunnel-coupled quantum wells (QWs), in which the emission of light quanta occurs when an electric field is applied as a result of cascade transitions of free carriers between subbands of size quantization in the process of downward relaxation in energy, and the mechanism for pumping radiating states is resonant tunneling. The emission wavelength in QCL is completely controlled by the size quantization of charge carriers; unlike traditional injection lasers it is not related to the band gap of the material and can vary by changing the width of quantum wells in the active region of the structure. Such lasers operate on majority carriers and are, in principle, unipolar devices.

The invention of QCLs was preceded by the theoretical prediction of R.F. Kazarinov and R.A. Suris relating light amplification and laser generation due to intersubband optical transitions in quantum wells excited as a result of resonant tunneling of electrons under electrical bias of the structure [10], made shortly after the discovery of superlattices (SL) by L. Esaki and R. Tsu [11]. The experimental implementation of the first QCL [8] was carried out only more than 20 years after the appearance of the fundamental results mentioned above, and for this it was necessary to solve a number of serious problems [12]. In particular, it was necessary to develop special SLs that play the role of an electron Bragg filter, which made it possible to significantly suppress the unwanted tunneling of electrons into neighboring quantum wells from upper laser states and, thereby, achieve the ratio of electron lifetimes at laser levels necessary to obtain population inversion. Besides, it was necessary to minimize the influence on the energy levels pattern of the space charge caused by free carriers injected into the structure. QCLs appeared as a result of many years of studies in the field of molecular beam epitaxy (MBE) and studies in the field of engineering the energy bands structure, wave functions of free charge carriers, probabilities of optical transitions, tunneling probabilities, probabilities of charge carrier scattering on phonons in low-dimensional systems [12–16].

Figure 1 schematically shows the conduction band diagram of one of the sections of the 25-period (active region plus electron injector region) quantum cascade structure (QCS) AlInGaAs|InP in electric field ~ 100 kV/cm, in which laser generation was obtained at wavelength of $4.26\,\mu$m [8]. The structure was grown by MBE method. The active region of the QCL structure contains 3 QWs and 4 barriers of different widths. Laser generation in such structure occurs according to a four-level scheme, which is used to describe the generation mechanism in many gas and solid-state lasers. Population inversion is achieved between the excited states $n = 3$ and $n = 2$ in the active region of the QCS, the energy gap between which is 295 meV according to calculations. The time of spontaneous emission transitions between the states $n = 3$ and $n = 2$ (indirect optical transitions in coordinate space) is ~ 13 ps. $n = 3$ state, localized mainly in QW 8 Å wide, is pumped by electrons tunneling through AlInAs barrier 45 Å thick from the region containing AlInAs|GaInAs SL with a variable effective band gap (SLVBG), which acts as an injector. The period of such SL is constant, but in the direction X the ratio of the QW width and the barrier changes, which leads to an effective band gap varying in the direction X (digitally graded alloy). The effective band gap in the SLVBG increases during transition towards X from left to right. Besides, to minimize the space charge effects during electron injection, the SLVBG region is doped with

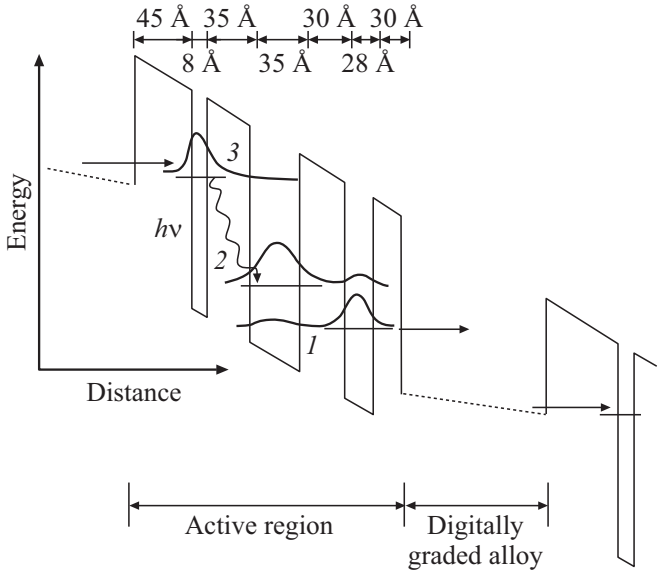

Figure 1. Schematic diagram of the conduction band of AlInGaAs|InP quantum cascade structure, in which laser generation was achieved at wavelength of 4.26 μm [8]. The distribution of the squared absolute values of the wave functions of states 1, 2 and 3 is also shown schematically.

silicon (donor-type impurity). According to calculations [8], in the electric field $\sim 10^5$ V/cm the SLVBG regions turn out to be quasi-neutral with an almost flat bottom of the effective conduction band (see Figure 1). Electrons relax in energy in the SLVBG region, and then are tunnel-injected into the $n = 3$ state of the active region. According to estimates [8], the characteristic time of such tunneling is ~ 0.2 ps, and the time of transitions from the state $n = 3$ to the state $n = 2$ with phonon emission (the main channel of nonradiative relaxation of the state $n = 3$) is ~ 4.3 ps in the field $\sim 10^5$ V/cm. The probability of transitions from the state $n = 2$ to the state $n = 1$ (the energy gap is 30 meV) with the emission of phonons turns out to be high due to the strong overlap of wave functions and the small difference in values of quasi-momentum of electrons in these states, and the corresponding transition time is ~ 0.6 ps. The time of electron tunneling exit from the state $n = 1$ to the SLVBG region is also small and amounts to ~ 0.5 ps. The ratio of the above energy relaxation times leads to the appearance of the population inversion between the states $n = 3$ and $n = 2$ and, accordingly, to laser generation.

Further, other laser generation schemes were implemented in the QCS for the mid-IR range (see, for example, the review [12]), with a different number of QWs in the active region, both with spatially -indirect and direct optical transitions. Lasers have been created that have a sufficiently high output power, operate at room temperature, both in pulsed and continuous mode, and emit in the region from 3.4 to 19 μm [12].

2.1.2. Quantum cascade THz lasers

The methods and approaches developed during the creation of QCLs in the mid-IR range made it possible to create THz QCLs. The first THz QCL uses a band scheme with so-called chirped SL in the active region of the structure. Laser generation at a frequency of 4.4 THz (wavelength 68 μm) with a peak power of the order of 2 mW (at 8 K) was obtained in a pulsed mode with a threshold current density of the order of several hundreds of A/cm^2 and was observed up to temperatures about 50 K.

Figure 2 schematically shows the fragment of structure of conduction band of such THz laser in electric field 3.5 kV/cm. Period of QCS contains 7 Qws GaAs with different width separated by barriers $Al_{0.15}Ga_{0.85}As$, also with different width. The structure was grown by MBE method on GaAs substrate. In total, the structure contains 104 periods. The active region contains three strongly tunnel-coupled QWs, and the injector region contains four QWs. According to the results of the paper [9], the laser generation occurs during spatially direct optical transitions through a mini-band gap about 18 meV between states 2 and 1 in the second and first mini-bands, respectively. Electrons in the injector resonantly tunnel into the upper laser state 2 from the ground state g. The lower laser state 1 is strongly coupled with a wide mini-band (width about 17 meV [9]) in the injector region, which ensures its rapid depletion due to the electrons transition to the first mini-band of injector. Numerical calculations [9] using the Monte Carlo method, solving three-dimensional Boltzmann equations taking into account the relaxation of electron energy due to the electron-phonon and electron-electron mechanisms showed that the time necessary for electrons to enter states 2, τ_2, is 0.8 ps, time of spontaneous transition between states 2 and 1 (transition with emission of acoustic phonon), τ_{21}, is 8.3 ps, and time of depletion of state 1, τ_1, is 2.5 ps. Due to the use in active region of a structure with an chirped SL τ_{21} is much higher than τ_2. Thus, $\tau_1 < \tau_{21}$, which is a necessary condition for achieving the population inversion between states 2 and 1. Additionally according to calculations [9] the population inversion occurs only when electron-electron scattering is taken into account, and, accordingly, when there is a significant concentration of non-equilibrium electrons in the active region of the structure.

The important feature of the THz QCL is the design of the laser waveguide, which ensures localization of the THz laser mode in the region where the population inversion is created, that is, in the region with the grown SL. In the paper [9] a so-called surface-plasmon (SP) waveguide was used, they (surfase-plasmons) are excited in the region between n^+-GaAs layer (buried lower contact layer) with electron concentration $2 \cdot 10^{18}$ cm^{-3} and 800 nm thick grown between the substrate and SL, and n^+-GaAs layer with electrons concentration $5 \cdot 10^{18}$ cm^{-3}, 200 nm thick, which ends the growth structure, and which also serves as the upper contact layer. This made it possible to

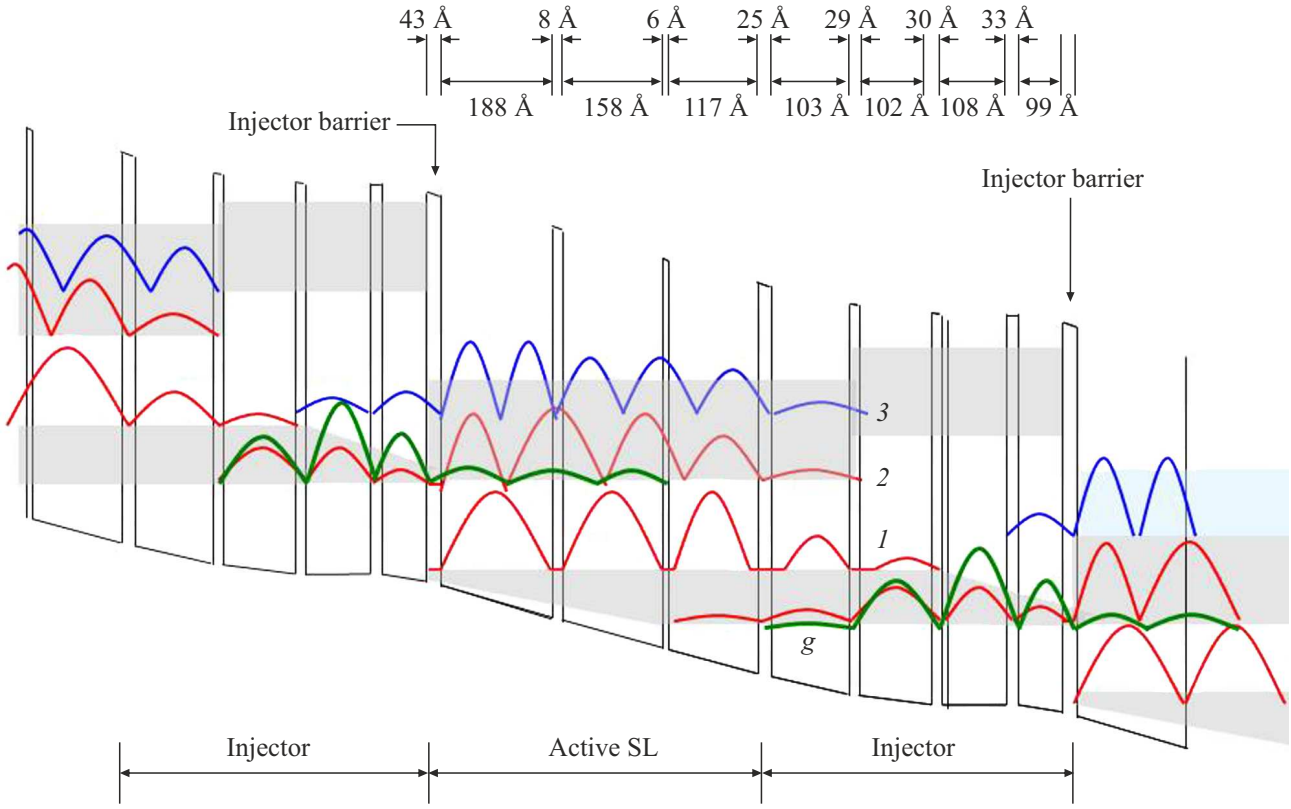

Figure 2. Fragment of the conduction band structure of the first THz QCL (calculated data for electric field strength of 3.5 kV/cm [9]). The squares of absolute values of the wave functions of the states (1, 2 and g) that are most important for achieving laser generation are also shown schematically. Shaded regions correspond to mini-zones of SL. The quantum well (QW) 102 Å wide in injector was doped with silicon to level $4 \cdot 10^{16}$ cm^{-3}.

concentrate the laser mode in layer with SL having thickness about 10 μm with a limiting factor Γ, characterizing the degree of overlap of the laser mode field with the region with population inversion, about 0.47, which facilitates the achievement of THz laser generation. It is also important that the SP wave excited in such waveguide is weakly overlapped by the buried lower contact layer n^+-GaAs, and is concentrated mainly in the specially undoped GaAs substrate, which minimized THz-radiation absorption on free carriers [9].

The growth structure was processed into a strip laser with a resonant cavity length of 1.24 mm and width of 180 μm. Laser mirrors were created by cleaving the structure along planes [110]. Special coatings for laser mirrors were not used in paper [9].

2.1.3. Existing approaches to the creation of quantum-cascade THz lasers

The demonstration of the first THz QCL in [9] stimulated a rapid growth of studies in this direction. After some time, works relating THz-QCLs started in many laboratories. The main efforts were aimed at achieving other generation frequencies in the THz region, increasing the radiation power and increasing the operating temperature.

Currently, THz-QCL structures are grown using both MBE [17–19], and metal-organic chemical vapor deposition (MOCVD) methods [20–23]. As a rule. the active region of quantum cascade THz lasers consists of hundreds of repeating periods, alternating QWs (each period includes a pair of states responsible for laser THz generation) and one or two injection/extraction sections. All periods contain doped sections to maintain the constant electric field throughout the active region of the structure. Currently, THz QCLs cover the frequency range of 1.3 to 5.4 THz (without strong magnetic field use) [19]. Lasers were created with a frequency tuning range about 0.65 THz at single-frequency generation with a central frequency ~ 3.47 THz [24]. A peak radiation power about 2 W was achieved in the pulsed mode at 58 K [25]. The wide frequency tuning range of THz generation and high output power of THz QCLs make it possible to use them in THz visualization of various objects, in THz spectroscopy, and also in THz communication [26]. The paper [27] demonstrated the operation of GaAs|AlGaAs THz QCL in the pulsed mode with maximum operating temperature of 250 K and generation frequency about 4 THz. This temperature record remained for two years. Recently, it was reported that maximum operating temperature about 261 K was achieved for THz QCL [28]. Such operating

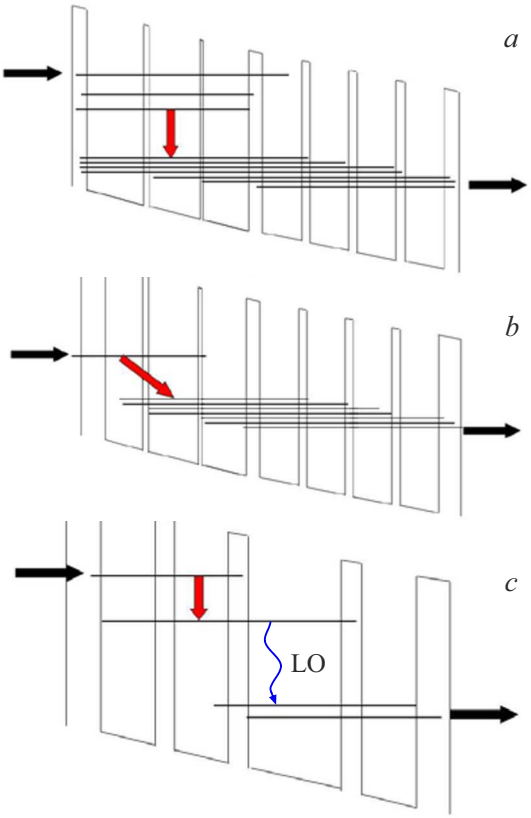

Figure 3. Schematic diagrams of THz-QCL active region with CS (*a*), BTC (*b*) and RP (*c*) designs.

temperatures make it possible to create compact THz lasers with single-stage thermoelectric cooling, which makes them very convenient for practical use.

The quantum design of the active region of the THz-QCL structure is one of the key factors determining the THz generation frequencies and operating temperatures. There are three main quantum designs for the active region of THz-QCL (Figure 3). This is primarily a scheme with an irregular SL (chirped superlattice, CS) (Figure 3, *a*), which was used in the first study relating THz-QCL [9]. An alternative design based on the so-called scheme of transitions bound state –continuum state (bound-to-continuum, BTC) (Figure 3, *b*) was proposed in [29], and was further used in a number of subsequent papers (see [19]). BTC design of the active region of THz QCL made it possible to significantly improve the parameters of THz QCL in comparison with those achieved in [9]. In particular, the operating temperatures were increased and the power of THz generation was increased (see [19]). An interesting design for the active region of THz QCL was proposed and implemented [30], in which the lower laser level is depleted due to processes involving the emission of optical phonons. i. e. scheme of resonant-phonon transitions (resonant-phonon, RP) (Figure 3, *c*). There are other options for the quantum design of the active region of THz QCL, which are variations of the schemes given above (Figure 3). For example, a quantum design of the active region of THz QCL was proposed and implemented, in which the pumping of the upper laser level and depletion of the lower one is accompanied by processes with the emission of LO phonons (the so-called phonon–photon–phonon scheme) [31]. New schemes were also proposed, but they were considered only theoretically so far (see [19] and other references there).

Currently, the best parameters were achieved for lasers with RP design of active region. THz QCLs with RP design can contain four, three, or even two quantum wells in the active region. Thus, in THz laser with operating temperature of 250 K [27] the active region (and, accordingly, the QCS period) contains two GaAs QWs with width of 72 and 144.9 Å, separated by barrier $Al_{0.3}Ga_{0.7}As$ 18.7 Å wide, and the injection barrier $Al_{0.3}Ga_{0.7}As$ is 33.7 Å thick. Laser generation at frequency about 4 THz in such structure occurs according to a three-level scheme, with the lower laser level being depleted due to electron transitions to lower energy level with the emission of LO phonons. Such a low-lying energy level, in turn, serves as an injector for pumping the upper laser level in the next QCS period. Optimization of the design of the active region in QCS used in the paper [27], recently made it possible to achieve the operating temperature of 261 K for GaAs|AlGaAs THz QCLs [28].

In THz QCL with high operating characteristics (high output power, low threshold currents and elevated operating temperatures) double metal waveguides are used for good localization of the THz laser mode in the active region of the structure. In such waveguides the epitaxial structure with quantum wells is located between two metal layers (for example, between Au, Ti|Au or Cu [19] layers, it is also possible to use Ag layers [32]). To create such laser structures the separation of growth structure with metal-coated upper contact layer from the substrate is used, it is turned over, and then transferred and welded to the surface of a metal layer on another substrate (receptor substrate), followed by applying a contact layer of metal to the top surface of „sandwich“ created in this way (flip-chip or metallic wafer-bonding technology [33,34]). In waveguides of this type frequency-independent values of the limiting factor $\Gamma \approx 1$ [19] are achieved, which also helps to reduce the radiation absorption on free carriers in the laser structure and lower the laser generation threshold.

The decrease in THz-QCL radiation power and the complete loss of generation in structures based, for example, on GaAs|AlGaAs with temperature increasing is mainly determined by the efficient electron-phonon interaction typical to such polar crystals as materials A_3B_5 [17]. The quantum design of THz-QCL is usually developed in such a way that the energy of optical transitions, and, accordingly, the energy gap between the subbands of the upper and lower laser levels are significantly lower than the energy of the LO phonon. This design prevents depletion of the upper laser level due to electron scattering processes with the emission of LO phonons at low (helium) temperatures.

However, at elevated temperatures, electrons in the upper-level subband can acquire kinetic energy in QW plane sufficient for scattering with the emission of polar LO phonons. Such processes reduce the population inversion with temperature increasing and lead to complete loss of laser THz generation, when the gain in the laser medium becomes less than the optical losses in the structure. To overcome this fundamental limitation of the laser generation temperature range in THz QCL, it was proposed to use nonpolar materials to create laser structures, namely Ge|SiGe quantum wells (see [35] and other references there). In such materials the electron-phonon interaction is determined by a short-range deformation potential and is significantly weaker in comparison with the long-range Fröhlich interaction mechanism. The material system Si–Ge is also interesting in that it has no single-photon absorption of light by optical phonons („restrahlen band"), and could potentially make it possible to obtain laser transitions with frequencies above 6 THz.

In the paper [35] THz laser based on Ge|SiGe *n*-type QCS was theoretically considered. The model laser contained 4 QWs in the active region, and its operation was assumed according to BTC scheme previously used in GaAs|AlGaAs QCL with a similar design of the active region [36] with the maximum temperature of the THz laser generation about 150 K. Numerical calculations demonstrate that Ge|SiGe QCS is less sensitive to temperature rise compared to GaAs|AlGaAs, and if optical losses of no more than $20\,\text{cm}^{-1}$ are ensured in the laser waveguide, then in Ge|SiGe QCS the laser THz generation is possible up to temperatures about 300 K.

Despite the interesting theoretical results, partially noted above, laser THz generation in SiGe-based QCS was not yet achieved. Only low-temperature spontaneous THz electroluminescence was observed experimentally in QCS Si|SiGe of *p*-type [37] and Ge|SiGe of *n*-type [38], caused by intersubband optical transitions.

2.1.4. THz quantum cascade lasers with high operating temperatures

Currently, the best parameters were achieved for THz QCLs based on GaAs|AlGaAs heterostructures obtained on GaAs substrates. Other systems of materials that are promising for creating THz QCLs with high operating temperatures were also studied. THz QCLs based on InGaAs|AlInAs [39], InGaAs|GaAsSb [40] and InGaAs|AlInGaAs [41] heterostructures grown on InP substrates were demonstrated, with maximum operating temperatures in the range 140–150 K. GaN|AlGaN heterostructures seem to be interesting from the point of view of the possibility of creating THz QCLs with high operating temperatures and generation frequencies above 5 THz. In heterostructures of this type, the discontinuity in the conduction band can exceed 1.5 eV, which makes it possible to create QWs that are much deeper compared to GaAs|AlGaAs heterostructures. Besides, due to the high optical phonon energy (90 meV versus 36 meV for GaAs), the temperature depletion of the upper laser levels in THz QCLs can be significantly suppressed. The paper [42] reported the observation of laser THz generation in the region of 5.4–7 THz in pulsed mode at temperatures 5.2–5.8 K in GaN|AlGaN quantum cascade structure grown on sapphire. However, this paper did not receive further continuation.

Note the interesting results obtained on InAs|AlSb QCS grown on *n*-InAs substrates. In structures of this type laser generation was obtained in pulsed mode with wavelength of $25\,\mu$m (12 THz) at a maximum operating temperature of 240 K [43]. In the paper [44] the same team of authors demonstrated continuous operation of QCL with wavelength of $20\,\mu$m (15 THz) at temperature of 240 K and laser operation in pulsed mode at temperatures up to 380 K. The radiation of lasers demonstrated in [43,44] can be classified as terahertz, since, as mentioned above (see Introduction), the boundary between THz and mid-IR ranges is quite arbitrary.

An alternative approach to the creation of THz QCLs with operating temperatures up to room temperature was proposed in the paper [45]. The approach is based on the difference-frequency generation (DFG) effect in the structure of mid-IR dual-frequency QCL (THz-DFG-QCL). The paper [45] demonstrated QCL operating at wavelengths $\lambda_1 = 7.6\,\mu$m and $\lambda_2 = 8.7\,\mu$m, and simultaneously generating THz emission with wavelength of $60\,\mu$m (5 THz). The laser structure based on GaInAs|AlInAs quantum wells was grown on InP substrate. The structure period contained two sections responsible for laser generation with wavelengths λ_1 and λ_2. Besides, the quantum design of the active region was organized in such a way that due to intersubband transitions in the structure, the frequency of which is close to the difference frequency of pump waves 1 and 2, the second-order nonlinear optical susceptibility $\chi^{(2)}$, responsible for generating the difference frequency, increases significantly. As a result, the value of $\chi^{(2)}$ at the THz frequency was increased by 2–3 orders of magnitude compared to the values typical for bulk nonlinear optical crystals. Generation of THz emission in the first THz-DFG-QCL [45] was observed up to temperatures about 150 K, and the efficiency of THz generation (or the efficiency of conversion of mid-IR radiation to THz) did not exceed $50\,\text{nW/W}^2$. Further, significant progress was made in Thz-DFG-QCL technology (see, for example, the review [18]). Measures were taken to ensure phase matching between IR and THz waves by THz wave output at a Cherenkov angle to the direction of propagation of IR waves (noncollinear phase matching). Further improvement of THz-DFG-QCL technology made it possible to significantly increase the efficiency of nonlinear conversion of IR radiation to THz (up to values about $0.3\,\text{mW/W}^2$ [18]). THz-DFG-QCL operating at frequency 3.5 THz at 300 K wit output power up to 2 mW was demonstrated [46].

2.2. THz lasers based on impurity intracenter transitions

It is known that at helium temperatures the capture of free carriers by ionized shallow impurity centers in semiconductors (this process can also be called the recombination of free carriers with ionized impurities) is accompanied by the appearance of THz emission [47]. Radiation occurs during the energy relaxation of charge carriers, under optical transitions between impurity levels. Radiative THz transitions between impurity levels occur in parallel with nonradiative ones (with the emission of phonons), which, of course, dominate, but, nevertheless, the fact of the existence of intracenter THz emission is well established. Intracenter THz emission was observed and studied in many studies [48–54], performed on various semiconductor materials, in which THz emission was excited as a result of impact ionization of impurity centers in the electric field.

2.2.1. Laser on resonance states

The appearance of stimulated THz emission in uniaxially deformed germanium of *p*-type (Ge(Ga)) under the influence of a strong electric field was discovered. Stimulated emission was observed at the temperature of liquid helium, when pressure about 4−9 kbar (in [100] or [111] direction) and pulsed electric field with strength about 2−4 kV/cm in geometry $E \parallel P$ were applied. Stimulated emission was explained by the population inversion of acceptor impurity levels formed from the acceptor ground state split by deformation, when one of the levels appears in the continuous band spectrum, i. e. becomes resonant [57]. In later papers [58,59] the model of THz laser based on resonant states (RLS) was developed. Figure 4 shows a diagram of subbands of the valence band and the energy levels of the acceptor impurity in uniaxially deformed Ge, which explains the operating principle of the THz-LRS.

Uniaxial deformation removes the degeneracy of the Ge valence band at $k = 0$ and splits it into two subbands with moment projections $m_z = \pm 3/2$ and $m_z = \pm 1/2$ onto the axis *Z*. The magnitude of such splitting is proportional to pressure and is about 4 meV/kbar for $P \parallel [111]$ [57]. The degenerate state of the acceptor also splits into two states, the energy difference of which increases with pressure increasing. Starting from a certain pressure value, the split-off state of the acceptor falls into the continuous spectrum and becomes resonant. In the case of deformation in [111] direction, the state split off from the ground state of the acceptor enters the continuous spectrum of the light hole subband at pressure about 4 kbar [58]. In this case, the ground state of the acceptor (lowest in energy) remains in the band gap. As a result, at high pressure in the band gap and in the continuum two series of impurity states related to split valence subbands are formed (Figure 4).

The electric field applied to the crystal ionizes impurity centers and depletes them, resulting in the formation of an ensemble of non-equilibrium holes in the valence band.

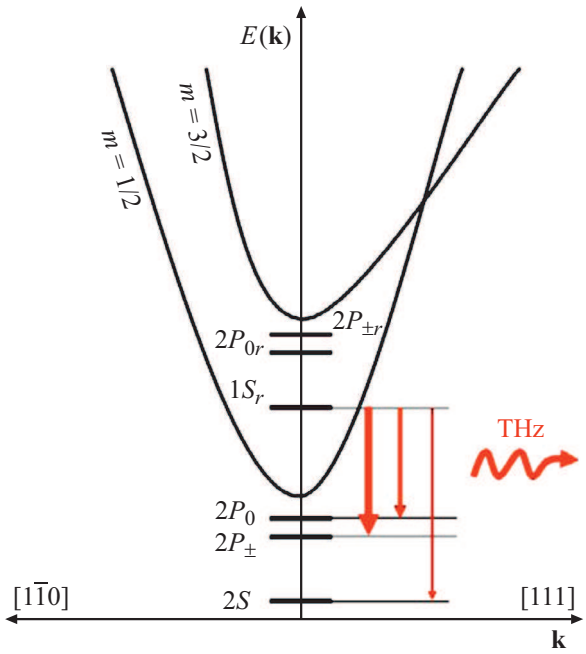

Figure 4. Scheme of energy levels of shallow acceptor and subbands of valence band for germanium crystal deformed in [111] direction at high pressure. The arrows indicate intracenter optical transitions responsible for laser THz generation [58,59].

Strong resonant scattering on acceptors of non-equilibrium holes with energy near the energy ε_0 corresponding to the position of the resonance level $1S_r$ (Figure 4) leads to the holes capture by this resonant state. At a sufficiently high electric field strength a sharp maximum appears in the hole distribution function near the energy ε_0. This leads to the population inversion appearance between the resonant and local energy levels of the acceptor[58,59]. According to calculations [58,59] the most probable optical transition responsible for laser THz generation is the intracenter transition $1S_r \rightarrow 2P_\pm$ (Figure 4). $1S_r \rightarrow 2P_0$ and $1S_r \rightarrow 1S$ transitions also ensure contribution, and the latter transition is not forbidden [58]. On deformed in the [111] direction *p*-Ge crystals with optically polished faces, for which achieved parallelism of the faces was at least 0.5−4 arcmin, the laser THz -generation in pulsed mode in the region of 5 to 10 THz, tunable by deformation was achieved [60]. Note that papers [61,62] contained data on observations of laser THz generation according to LRS mechanism in stressed quantum wells SiGe|Si doped by acceptors. THz emission was excited by applying pulsed electric bias to the structures. Moreover, the electric field with a strength of 300 −1500 V/cm was directed parallel to the QW plane.

A laser based on resonant states makes it possible to obtain THz generation in the frequency region [60], that is inaccessible to THz quantum cascade lasers based on, for example, GaAs|AlGaAs. However, such laser is fundamentally low-temperature device, requiring temperatures of liquid helium, and therefore its practical applications are extremely limited.

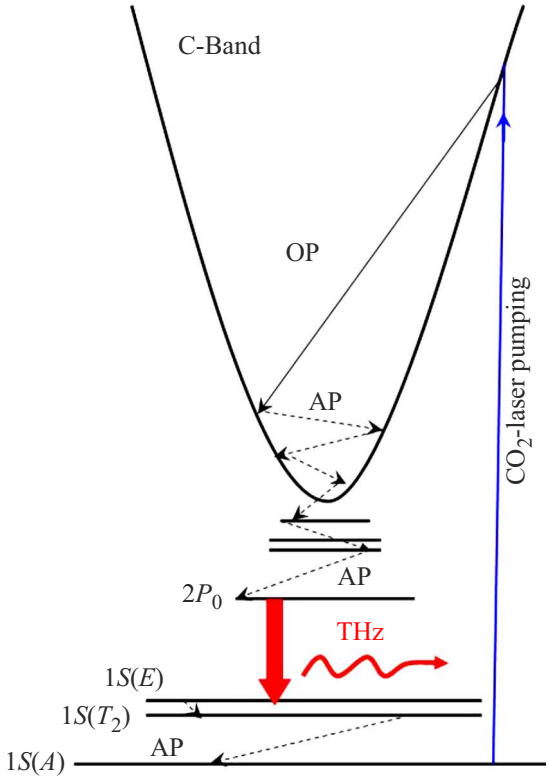

Figure 5. Scheme for formation of laser THz generation during photoionization of shallow donors in Si(P). The solid arrow corresponds to the transition with the emission of an optical phonon (OP), the dashed arrows correspond to the transitions with the emission of acoustic phonons (AP).

2.2.2. Laser with optical pumping of impurity-band transitions

Intracenter THz emission can also be excited as a result of the impurities photoionization by IR radiation. A version of THz laser based on intracenter optical transitions operating at helium temperatures was demonstrated on silicon crystals doped with phosphorus donors, during photoionization of the impurity by pulsed CO_2-laser radiation [63]. A Si(P) laser sample with donor concentration $(0.9–3) \cdot 10^{15}\,\mathrm{cm}^{-3}$ was prepared in the form of a rectangular parallelepiped with dimensions about $7 \times 7 \times 5\,\mathrm{mm}^3$. The opposite faces $7 \times 5\,\mathrm{mm}^2$ were optically polished and parallel to each other with an accuracy of 1 arcmin, thus forming a Fabry-Perot resonator. CO_2-laser pump radiation was incident normally on the face $7 \times 7\,\mathrm{mm}^2$ of the sample. Laser THz emission with wavelength of $59\,\mu$m (5.1 THz) was detected, corresponding to optical transitions $2\mathrm{P}_0 \rightarrow 1\mathrm{S(E)}$ (see Figure 5) in phosphorus donors. The threshold radiation power of the pump laser was about $10\,\mathrm{kW/cm}^2$. According to the results of the paper [63], the gain in such an intracenter THz laser on Si(P) is about $1\,\mathrm{cm}^{-1}$.

The mechanism for the appearance of intracenter population inversion during photoionization of the donor impurity in silicon is associated with the accumulation of non-equilibrium carriers in long-lived excited states of the impurity center. In the case of Si(P), such long-lived state turns out to be the state $2P_0$. Electrons ejected into the conduction band by CO_2-laser radiation relax downward in energy. Emitting at that optical phonon and a series of acoustic phonons (Figure 5), they end up near the bottom of the conduction band. Further, the relaxation process proceeds along the ladder of impurity levels with the emission of acoustic phonons only. In this case, the probability of acoustic phonons emission decreases with increasing of wave vector of the phonon (and, accordingly, with energy increasing of the emitted acoustic phonon). State $2\mathrm{P}_0$, where the electron comes from higher energy levels, emitting acoustic phonons, is spaced away from the underlying sublevels of the donor ground state 1S(E), $1\mathrm{S}(\mathrm{T}_2)$ and 1S(A) by 21.1, 22.4 and 34.1 meV, respectively [64]. So, further electrons relaxation from the state $2\mathrm{P}_0$ to sublevels of the ground state of the donor with the acoustic phonons emission is difficult. Calculations [63] show that the lifetime of the state $2\mathrm{P}_0$ is about $1.5 \cdot 10^{-8}$ s at 5 K. In this case, the lifetime of the state 1S(E) turns out to be significantly shorter and is about $2 \cdot 10^{-10}$ s, due to the fact that the energy gap between this state and the sublevels of the ground state of the donor $1\mathrm{S}(\mathrm{T}_2)$ and 1S(A) is small and allows transitions between states with the acoustic phonons emission. As a result, a four-level THz laser generation scheme is actually implemented. Further, THz laser generation was obtained by photoionization of other donors also in silicon (Sb, As, Bi) [65,66]. Laser THz generation was also demonstrated during resonant intracenter optical excitation of donors in silicon [67].

THz silicon laser with optical pumping of impurity-band transitions makes it possible to obtain THz generation frequencies that are difficult to achieve in THz QCLs. Thus, in Si(Bi) when pumped by line 9R20 ($9.6\,\mu$m) of CO_2-laser radiation the generation was obtained at THz frequencies of 5.74 and 6.17 THz, and during pumping by line 10P20 ($10.6\,\mu$m), the generations were also obtained at frequency of 6.34 THz [65]. At the same time, such THz laser, like laser based on resonant states, requires helium operating temperatures. Besides, THz laser installation on silicon with optical pumping from CO_2-laser with a helium optical cryostat for laser crystal becomes quite large. All this limits the practical application of such THz laser.

2.3. THz lasers based on interband transitions in narrow-gap semiconductors

2.3.1. Lasers based on PbSnSe(Te)

In direct-gap solid solutions of PbSnSe(Te) (lead-tin chalcogenides) the band gap can vary over a wide range depending on the composition and temperature, and can correspond to THz region of the spectrum [68]. Besides, such materials can be both *n*- and *p*-type of conductivity, and *p*–*n*-junctions can be created on their basis. Thus, these materials are, in principle, suitable for creating THz

lasers of the traditional type, the radiation in which is caused by the injection and interband radiative recombination of non-equilibrium electrons and holes. Based on the solid solution $Pb_xSn_{1-x}Se$ the injection THz lasers emitting at wavelengths 40 μm (7.5 THz) [69], 46 μm (6.52 THz) [70], and also 50.4 μm (5.96 THz) [71], and operating in the temperature range 4.2–80 K were demonstrated. However, the technology of PbSnSe(Te) materials is complex and underdeveloped. The residual concentration of free carriers in such materials remains very high (about 10^{17} cm^{-3} and higher). Using this system of materials, it is not yet possible to obtain high-quality structures with quantum wells, which are necessary to create the injection lasers with low threshold currents and high output power [72]. At the same time, at first glance, it seems surprising that in such narrow-gap materials with high residual concentration of free carriers it is possible to obtain laser THz generation, since in such situation one would expect efficient nonradiative Auger recombination of non-equilibrium carriers. In the paper [73] attention was drawn to the fact that Auger recombination in PbSnSe(Te) turns out to be suppressed due to the symmetry between the laws of dispersion of charge carriers in the C- and V-bands.

2.3.2. HgCdTe-based lasers

In direct-gap HgCdTe materials it is also possible to change the band gap, E_g, within wide limits. E_g in such system can vary depending on the composition from practically 0 in HgTe (gapless semiconductor) to a value about 1.6 eV in CdTe. Therefore, this system of materials is of interest both for IR optoelectronics both in general and, and in particular, for creating radiation sources operating in the THz region of the spectrum. The complexities of the technology of these materials and, in particular, the problems in obtaining *p*-type of conductivity, coupled with the need for post-growth processing of materials [74], for a long time did not allow the creation of radiation sources based on them with acceptable characteristics. HgCdTe solid solutions were used mainly to create photodetectors in the mid-IR range in the region 8–14 μm. The use of MBE methods made it possible in the early 1990s to create the first injection IR lasers on double HgCdTe heterostructures with generation wavelengths up to 5.3 μm [75,76], operating at temperatures up to about 60 K.

In the last decade, MBE technology for the growth of structures with HgTe|HgCdTe quantum wells received significant development due to the rapid growth of interest in topological 2D insulators (or the quantum spin Hall effect) [77,78]. By changing the temperature, width and composition of quantum wells $Hg_{1-x}Cd_xTe|Hg_{1-y}Cd_yTe$ it became possible to control in wide range the energy of interband transitions, shift it to the region corresponding to quanta of the mid-IR and THz ranges (see [79] and other references there).

Studies of radiative recombination of nonequilibrium carriers in structures with HgCdTe quantum wells under intense interband photoexcitation were carried out in papers [80–82]. In paper [80] structures with HgTe|HgCdTe quantum wells grown by MBE method on (013) GaAs substrate were studied. Five QWs were enclosed in a wide-gap HgCdTe waveguide. During optical interband pumping of structures with radiation with wavelength about 2–2.3 μm (an optical parametric oscillator was used), the stimulated emission (SE) was obtained with wavelength of 19.5 μm (15.4 THz) at 20 K and threshold photoexcitation intensity about 5 kW/cm^2. The studied samples did not have laser resonator, since the cleaving of the grown structure did not produce parallel opposite faces. Therefore, the observed SE was formed due to optical amplification in one pass. In the papers [81,82] in structures with quantum wells $Hg_{1-x}Cd_xTe|Hg_{1-y}Cd_yTe$, also enclosed in the wide-gap HgCdTe waveguide, the stimulated emission with wavelength of 31 μm (9.7 THz) was obtained at 8 K and excitation by radiation of pulsed CO_2-laser (threshold photoexcitation intensity was about 45 kW/cm^2). As a result of comparing experimental data and theoretical calculations, the authors of the papers [79–82] concluded that in quantum wells $Hg_{1-x}Cd_xTe|Hg_{1-y}Cd_yTe$ with a low cadmium content ($x < 0.1$) and small band gap ($E_g < 140$ meV) the Auger-recombination of non-equilibrium electrons and holes is suppressed, which makes it possible to obtain SE on interband transitions. The suppression of the Auger-recombination is due to the manifestation of the quasi-relativistic dispersion law of electrons and holes, implemented in this type of quantum wells [79–82]. Further development of the technology of HgCdTe materials and device structures based on them will possibly allow to create based on QW $Hg_{1-x}Cd_xTe|Hg_{1-y}Cd_yTe$ lasers in THz range and with electrical excitation (injection lasers).

Note that in the paper [83] a theoretical model was constructed that allows one to calculate the characteristics of lasers based on QW $Hg_{1-x}Cd_xTe$ with optical or electrical excitation, which can probably be created in the future. It was shown that for such THz lasers it is preferable to use a narrow QW with a composition corresponding to the binary compound HgTe and width less than the critical value, d_{cr} equal to 6.3 nm (0 K) and 7.4 nm (77 K), at which there is a transition from the inverted structure to the normal structure of the zones [83]. It was also shown that the longest wavelength of laser THz generation in such a laser can be 50 μ m ($\sim$ 6 THz) at 77 K, and the threshold current density in this case can be by two orders of magnitude lower than in existing QCLs.

2.4. THz laser on *p*-Ge in crossed strong electric and magnetic fields

In the early 1980s a number of papers reported the detection of stimulated THz emission and THz laser generation in *p*-Ge crystals in strong crossed electric and magnetic fields at helium temperatures[84–89]. Numerous experimental and theoretical studies made it possible to establish that laser generation in the region of 1 to 4.5 THz in *p*-Ge is caused

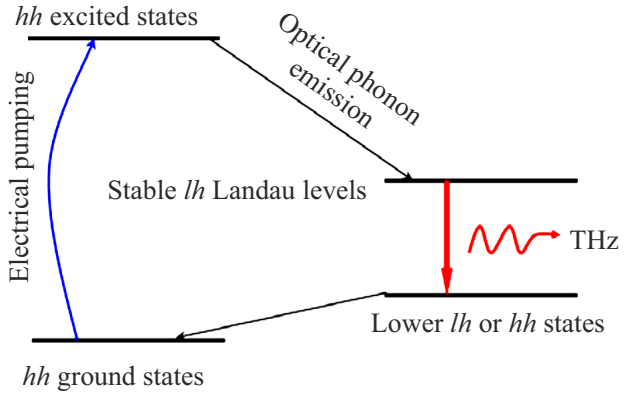

Figure 6. Diagram of optical transitions between states of holes with inverted population in the valence band *p*-Ge in crossed electric and magnetic fields.

by population inversion between the subbands of light and heavy holes (*lh* and *hh*, respectively) of the valence band that occurs when hot carriers move in the streaming mode in crossed electric field with a intensity E of 0.5 to 3 kV/cm and magnetic field with induction B of 0.5 to 2.5 T [90,91]. In this case, optical transitions between Landau levels within the *lh* subband, as well as transitions between Landau levels in the *lh* and *hh* subbands form the spectrum of THz emission (Figure 6).

The strong electric field applied to *p*-Ge sample ionizes acceptors and populates the valence band with free holes. At a certain ratio of the electric and magnetic fields ($E/B \approx 1-1.5$ kV/cmT), heavy holes accelerate during their drift and gain energy higher than the energy of the optical phonon ($\hbar\omega_{OP} \approx 37$ meV), after which their intensive scattering by optical phonons starts. Some of the heavy holes, emitting optical phonons, move into the subband of light holes. It is important to add that under these conditions, holes in the *lh* subband during their drift at the chosen ratio of the electric and magnetic fields do not reach the energy of the optical phonon, and therefore are scattered much weaker. Light holes are accumulated on closed (in momentum space) trajectories of motion with energy below the energy $\hbar\omega_{OP}$. As a result, the population inversion occurs between the subbands *lh* and *hh* (Figure 6). In magnetic field both hole subbands are split into discrete Landau levels. Due to the large effective mass of heavy holes and the short lifetime the Landau levels in the *hh* subband actually merge into one wide band. Holes in *lh* subband have a significantly longer lifetime and a significantly larger splitting between individual Landau levels. Therefore, THz laser generation occurs both on optical transitions between individual Landau levels in the *lh* subband, and on transitions between Landau levels in the *lh* subband and *hh* subband [92]. With amplitudes increasing of both electric and magnetic fields, the frequency of laser THz generation tends to increase.

Output pulse power of *p*-Ge-based THz laser can reach 5 W [93]. *p*-Ge-based laser with single-frequency generation and laser linewidth about 1 MHz [94] was demonstrated. The paper [92] reported on the achievement of modes self-synchronization in *p*-Ge-based THz laser with an external resonant cavity, in this regime the laser generated a series of pulses with individual pulses width about 100 ps.

At the same time, *p*-Ge-based THz lasers have a number of significant disadvantages that limit their use. Due to the features of the population inversion formation mechanism, such lasers operate at helium temperatures, require strong magnetic fields (usually magnetic field is created in a superconducting solenoid) and high voltages for electrical bias, and therefore require very good heat removal. In this case, pulsed power supply has a low repetition frequency and a low duty cycle (in the best case, the repetition rate is about 1 kHz, and the duty cycle is maximum 10^{-3} [95]).

2.5. THz emission during interband optical photoexcitation of semiconductors

2.5.1. Impurity THz photoluminescence

In terahertz technologies, in addition to THz lasers, the creation and operation of which is associated with certain difficulties, partially noted above, various sources of THz emission are required, including simpler ones, for example, emitters such as THz light-emitting diodes (LEDs). Relatively simple, high-speed electronic emitters of THz emission can be created using intracenter optical transitions in shallow impurities. As it was discussed above in Section 2.2, the intracenter THz emission was observed and studied in many papers under conditions of impact ionization or IR photoionization of impurity centers in semiconductors at low temperatures.

It was first shown in papers [96,97] that intracenter THz emission is also generated under conditions of interband photoexcitation of semiconductors doped with shallow impurities. Therefore, we can speak about impurity THz photoluminescence (THz PL). By now the impurity THz PL was observed in a number of bulk semiconductors [96–101], as well as in structures with QWs doped with shallow impurity centers [102–104]. THz photoluminescence can be quite intense. For example, in *n*-GaAs crystals at helium temperatures, the external quantum yield of impurity THz PL can reach 0.3% [97]. Therefore, this phenomenon can be applied in THz technologies.

The mechanisms of impurity THz photoluminescence are closely related to the processes of recombination of non-equilibrium carriers with the participation of impurity centers. Several specific microscopic mechanisms of impurity THz-PL can be indicated. For example, impurity Auger recombination of electrons and holes or bound excitons may be responsible for impurity THz PL (see Figure 7). In this case, the electron-hole pair or exciton recombines nonradiatively with excitation of bound carrier, for example, electron, into the conduction band. The subsequent capture

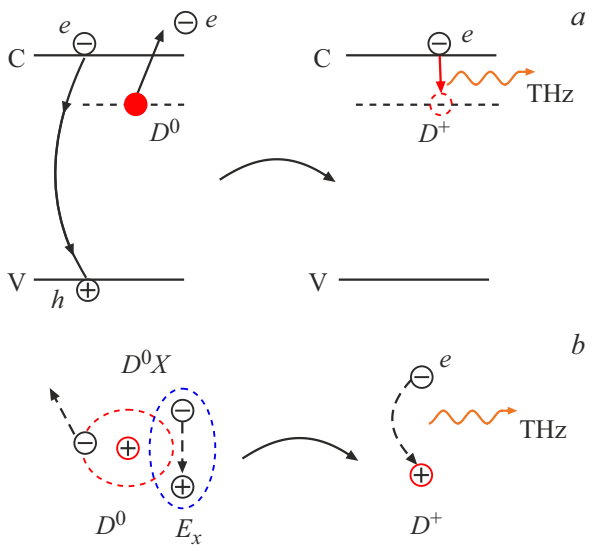

Figure 7. Formation of THz-PL during impurity Auger recombination. *a* — nonradiative recombination of electron with hole in doped semiconductor with the transfer of energy equal to about band gap to carrier bound to impurity (the bound carrier is depicted as a solid circle); *b* — nonradiative recombination of exciton bound on neutral donor, accompanied by the generation of free electron in the conduction band and ionized donor in the band gap.

of the free electron by an ionized impurity center is accompanied by THz emission. Another mechanism is closely related to the recombination of free holes with electrons on neutral donors — this is the so-called D^0h recombination (Figure 8). It can be radiative, and this type of recombination is well known for semiconductors such as GaAs (see, for example, [105,106]). Such recombination leads to the formation of charged donors and free electrons in the conduction band. Further, everything is very similar to the situation that occurs during the electrical breakdown of impurities: the capture of free electrons by ionized donors leads to THz emission. The latter mechanism causes THz photoluminescence in *n*-GaAs [97] and *n*-GaN [98] at low temperatures. As for the mechanisms corresponding to Figure 7, today there are no experimental data indicating the occurrence of such THz-PL mechanisms.

In recent paper [107] it was shown that in Si crystals doped with Li (a shallow donor in silicon with ionization energy about 33 meV [64]), at low temperatures the intracenter THz PL is excited as a result of the interaction of neutral donors with surface plasmons on droplets of electron-hole liquid (EHL). As a result of such dipole-dipole interaction, impurity centers are ionized, and the subsequent capture of free electrons by them produces intracenter THz emission (see Figure 9).

Such a „plasmon-impurity" mechanism for excitation of intracenter THz emission is efficient in situation where the energy of plasma oscillations in EHL droplets is close to or exceeds the ionization energy of the impurity center, which occurs in the case of EHL formation in silicon with lithium. It should be added that surface plasmons themselves on EHL droplets in silicon with an energy of about 34 meV (8.23 THz) do not emit [107–109], but as a result of their interaction with donors of lithium THz emission is generated. In these processes the impurity centers play the role of peculiar antennas that convert the near electromagnetic field of plasmons on EHL droplets into observable THz emission. In this case, a clear correlation is observed between the presence of lines of intracenter optical transitions in THz-PL spectra and the presence of EHL emission line in the spectra of interband recombination

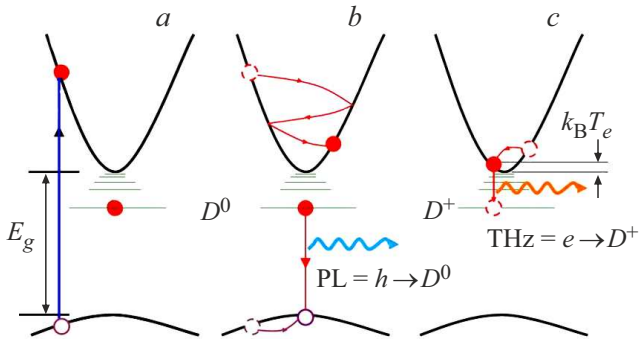

Figure 8. Scheme of generation of intracenter THz generationas as a result of D^0h-recombination. *a* — optical excitation of electron-hole pairs; *b* — relaxation of non-equilibrium carriers and recombination of free holes with electrons on neutral donors; *c* — THz emission transitions of electrons upon capture on ionized donors.

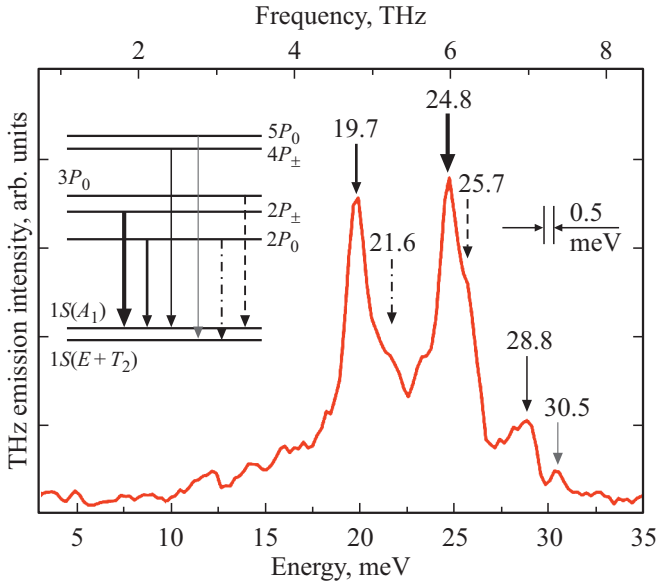

Figure 9. Characteristic THz-PL spectrum in Si (Li) at $T = 5$ K under conditions of interband photoexcitation by radiation with wavelength of 530 nm at photoexcitation density of 33 W/cm^2. The numbers indicate the transition energies in meV. The insert indicates specific intracenter optical transitions in lithium donors responsible for the observed THz emission.

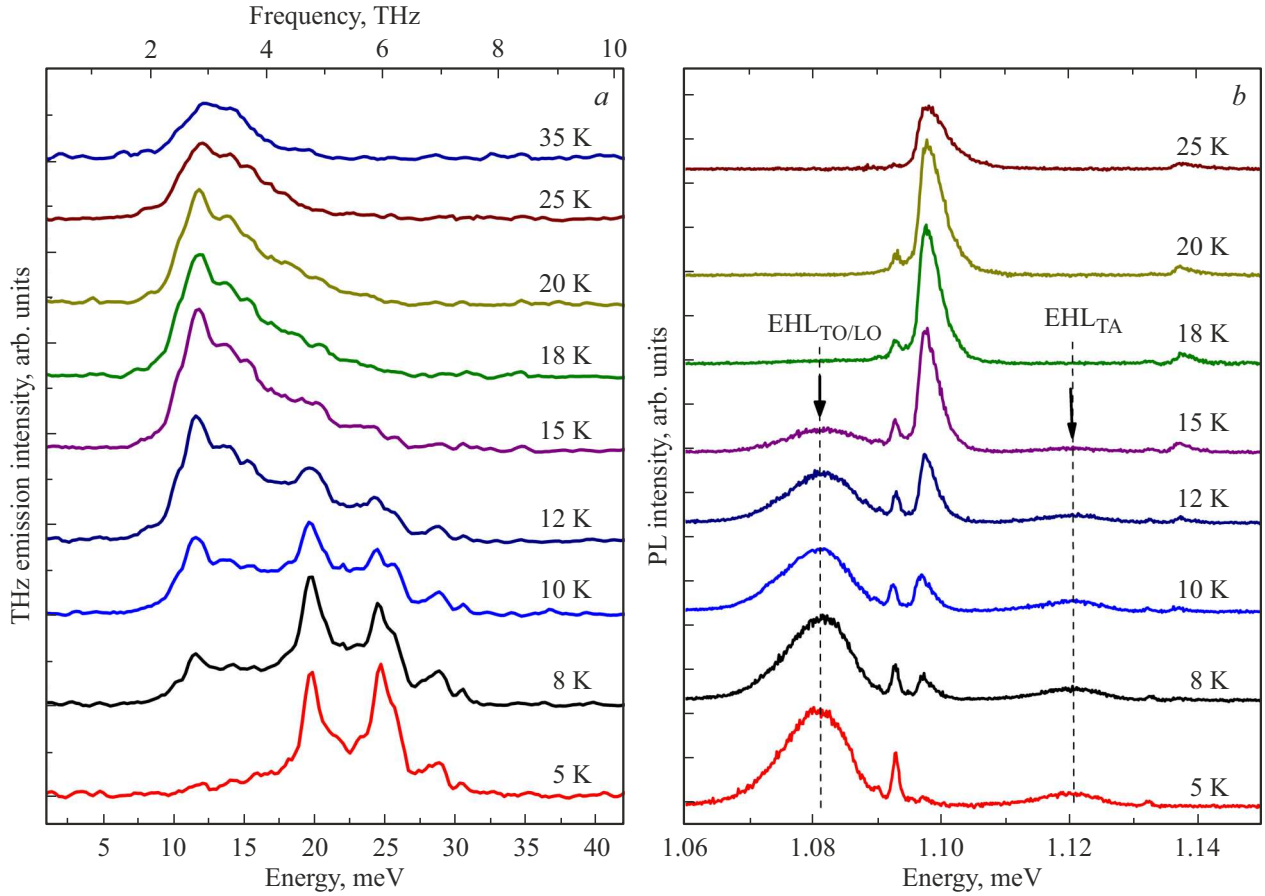

Figure 10. *a* — characteristic THz-PL spectra in Si (Li) crystals. Intracenter THz emission in lithium donors is concentrated in the region of energies about 17–31 meV (see also Figure 9). *b* — spectra of interband recombination radiation in Si (Li) crystals. Arrows show the position of radiative recombination lines in EHL droplets. The measurements were carried out under the same conditions: photoexcitation wavelength 530 nm, photoexcitation density 33 W/cm^2.

radiation in Si (Li) (see Figure 10). Such correlation is observed in a wide range of photoexcitation densities: from a few to about a hundred W/cm^2 [107]. Thus, intracenter THz emission in lithium donors is inseparably associated with the existence of EHL droplets in the crystal, and intracenter THz emission, in turn, can serve as a probe (detector) for the excitons condensation into EHL droplets [107].

In the THz-PL spectra in Figure 10, *a*, along with the lines of intracenter THz emission concentrated in the region of energies from 17 to 31 meV (from 4.1 to 7.5 THz), one can also see emission band with a maximum at energy about 11.6 meV (2.8 THz), caused by radiative THz transitions between the energy levels of free excitons [110], which will be discussed below.

2.5.2. Impurity THz emission caused by injection of non-equilibrium carriers in structures with $p-n$-junction (THz-LED)

In Section 2.5.1 the processes responsible for the generation of impurity THz emission during interband optical excitation of semiconductors doped with shallow impurities (THz-PL) were considered. Similar processes can lead to impurity THz emission under conditions of electrical injection of non-equilibrium charge carriers into doped material, for example, in structures with $p-n$-junction.

Impurity THz electroluminescence (EL) induced by electrical injection of non-equilibrium carriers was first obtained in the paper [111]. In fact, in this paper the THz LED was demonstrated for the first time. The experiments [111] were performed on planar 4H-SiC $p^+-n^--n^+$-structures obtained by method of chemical vapor deposition (MOCVD) on 4H-SiC (0001) n^+ substrates ($N_d - N_a \approx 2 \cdot 10^{18}$ cm^{-3}) (main impurity — nitrogen) 400 μm thick. The layer n^- had a thickness about 7 μm and was doped with nitrogen to the level $N_d - N_a \approx 5 \cdot 10^{15}$ cm^{-3}. The layer p^+ was created by aluminum diffusion into the epitaxial layer n^-, its thickness was about 100 nm, and the doping level $N_a - N_d \approx 5 \cdot 10^{19}$ cm^{-3}. Contact to p^+-layer was continuous. The contact to the substrate was circular and was applied at the periphery of the structure, leaving an uncovered area of size 1.5×2 mm^2 for THz emission output. The structure was mounted on the cold finger

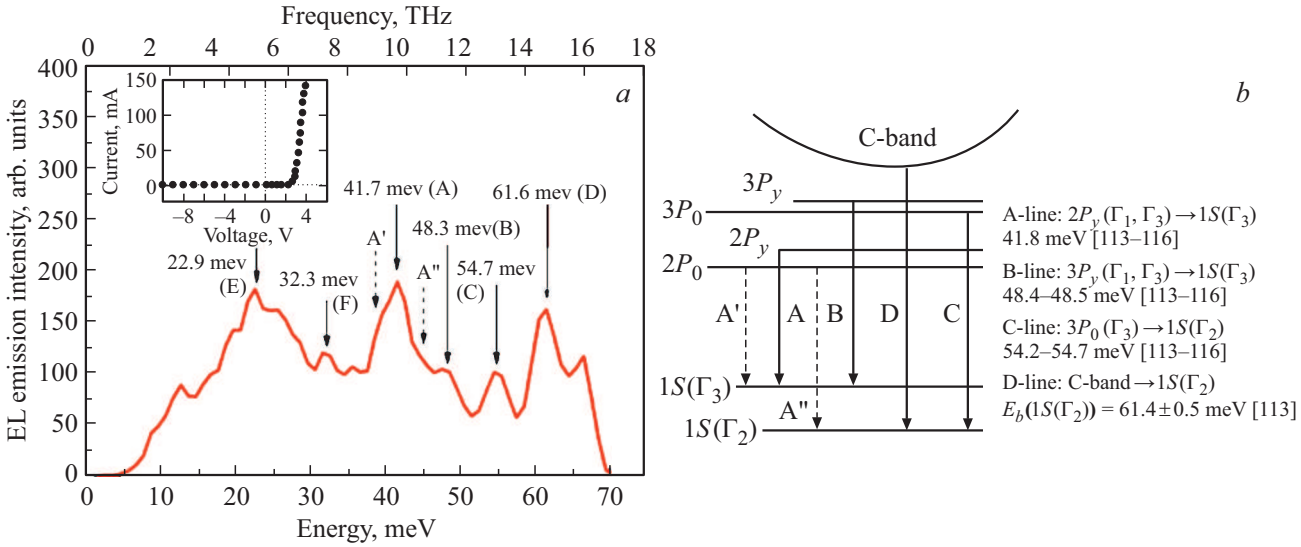

Figure 11. *a* — THz electroluminescence spectrum of 4H-SiC $p^+-n^--n^+$-structure at $T = 50$ K and forward current pulse amplitude 150 mA. The electrical bias was supplied in the form of rectangular pulse bursts, which followed with a frequency of 80 Hz. Each burst contained 10 pulses, and the pulse width and pause were 125 μs. This bias was chosen to minimize the influence of structure Joule heating on the measurement results. The insert shows the current-voltage curves of the structure at 50 K. *b* — scheme of intracenter optical transitions in nitrogen donors in hexagonal environment in 4H-SiC, forming THz-EL. The energies of transitions between states of the nitrogen donor, obtained from IR spectroscopy data of 4H-SiC [113-116], are also indicated here. The designations of impurity states are given in accordance with the classification of their symmetry [113].

of an optical cryostat with „p^+-layer down“ to improve heat removal. THz emission output was ensured through the substrate. The structures had acceptable current-voltage curves of the diode type over the entire range of temperatures studied (20 to 300 K) [111]. Since in the studied structures $p^+ \gg n^-$, then with forward bias there was almost one-sided injection — injection of holes into the *n*-region of the structure. It is important to add that the 4H-SiC material was chosen for the THz LED intentionally. The material is interesting in that the diffusion length of non-equilibrium holes in *n*-region is quite large and reaches tens μm [112], which is important for the THz-EL induced by injection. Besides, the high binding energy of impurities in 4H-SiC crystals makes it possible to observe impurity THz emission up to significantly higher temperatures compared to other materials, for example, GaAs, Ge or Si.

Figure 11 shows the characteristic spectrum of injection THz EL in the studied 4H-SiC $p^+-n^--n^+$-structures at temperature of 50 K and injection current of 150 mA. Figure 11, *b* shows a diagram of intracenter transitions responsible for lines A, B, C and D in THz-EL spectrum [111]. The spectral position of A-, B- and C-lines of THz emission is in good agreement with the energies of optical transitions from the excited states 3P and 2P to the sublevels of the ground state 1S of nitrogen donor in hexagonal environment, which were previously established on the basis of studies of absorption spectra and photoconductivity in 4H-SiC crystals[113–116]. The D-line can be attributed to optical transitions from the conduction band to the $1S(\Gamma_2)$ sublevel of the ground state of the donor, taking into account the known value of the bond energy of the nitrogen donor in 4H-SiC [113]. E and F lines in the THz emission spectrum at energies of 22.9 and 32.3 meV, respectively, were not accurately identified in [111], but very likely they are due to impurity optical transitions. In the emission spectrum in Figure 11, *a* a wide structureless background is also visible, which may be associated with the contribution of the hot carriers radiation (black body-like emission of hot carriers [111]). Hot carriers with an effective temperature T_{eff} exceeding the lattice temperature may well appear in the structure during injection. Mathematical modeling of the background and its subtraction from the observed THz-EL spectrum showed that the spectral position of THz emission lines A, B, C, D, E and F remains unchanged, and the integral intensity of lines of impurity THz emission exceeds the integral intensity of the background [111]. The binding energy of acceptor impurities in 4H-SiC ranges from 216 to 266 meV [117], and therefore intracenter optical transitions in acceptors should not contribute to THz-EL in the studied spectral range (Figure 11, *a*).

Intracenter optical transitions in nitrogen donors arise as a result of the free electrons capture by ionized donors. Such ionized donors, in turn, are generated in *n*-region of the structure as a result of the recombination of injected non-equilibrium holes with neutral donors, which are present in the quasi-neutral part of *n*-region at low temperatures. Free electrons enter the *n*-region of the structure from the electrical contact. This is required by the condition of electrical neutrality of *n*-region of structure. In fact, this

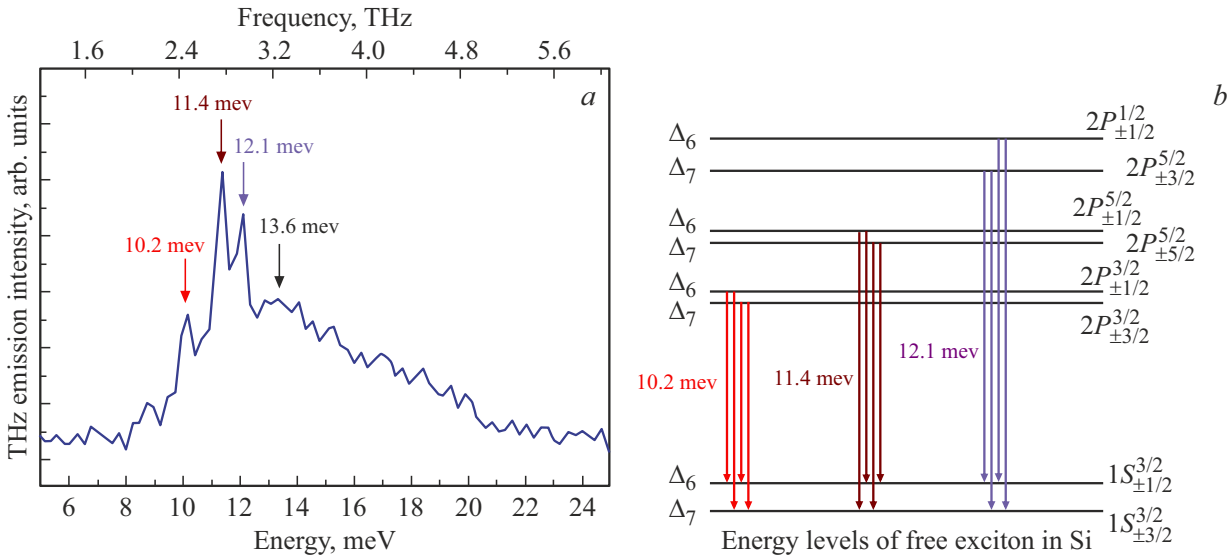

Figure 12. *a* — THz-PL spectrum in Si crystal with resistivity of $12\,\mathrm{k\Omega}\cdot\mathrm{cm}$ at $T = 5\,\mathrm{K}$ in conditions of stationary interband photoexcitation of the crystal with line 660 nm of semiconductor laser. Photoexcitation density $0.1\,\mathrm{W/cm^2}$. Spectral resolution 0.5 meV. *b* — diagram of the energy levels of free exciton in silicon. The arrows indicate three groups of optical transitions responsible for the lines with maxima at 10.2, 11.4 and 12.1 meV in THz-PL spectrum. The classification of exciton states is given in accordance with that used in the papers [120,121].

mechanism of THz-EL generation is similar to the mechanism of THz emission excitation, schematically shown in Figure 8 (conditionally, D^0h-mechanism). The only difference is in the method of generating non-equilibrium electrons and holes in material doped with shallow centers. In the paper [111] the mechanism of excitation of impurity THz-EL, caused by intracenter transitions in donor impurities, was also considered in the case of non-equilibrium holes injection into compensated material containing donor-acceptor pairs (conventionally, D–A-mechanism). Experimental data [111] do not allow authors to conclude which of the mechanisms (D^0h or D–A) of excitation of intracenter THz emission in $p^+-n^--n^+$-structures 4H-SiC predominates. Apparently, both one and the other mechanism take place.

In $p^+-n^--n^+$-structures 4H-SiC studied in the paper [111] THz EL was observed up to room temperatures. In this case, all the above-mentioned THz emission lines were preserved in the emission spectra. At 100 K the power efficiency for THz LEDs based on $p^+-n^--n^+$-structures 4H-SiC is about $5.4\cdot10^{-5}$, and the external quantum yield of THz emission reaches 0.7%. At injection current of 300 mA the THz emission power reached $58\,\mu$W (100 K) [111]. These results show that THz LEDs based on $p-n$-structures SiC can serve as rather simple, compact THz emission sources with acceptable output power and operating up to room temperatures. An optimization of the THz emission output from $p^+-n^--n^+$-structure 4H-SiC can significantly increase the output power of THz LEDs. Such sources may prove to be useful for applications in THz technologies. Note that observation of injection THz electroluminescence in $p-n$-structures based on silicon was reported in the paper [118].

2.5.3. Exciton THz photoluminescence

The processes of energy relaxation during binding of electrons and holes into free excitons and during the carriers capture by attractive impurity centers have much in common [119]. Therefore, one can expect that when non-equilibrium carriers are captured by excitons, optical THz transitions also take place between the levels of free exciton states, similar to intracenter optical transitions in shallow impurity centers. The paper [110] reported the discovery and study of exciton THz photoluminescence (PL) in Si crystals. Such THz-PL can also be attributed to the intrinsic THz-PL of the crystal, and impurity THz-PL can be attributed, accordingly, to the exctrinsic THz-PL. The experiments [110] were carried out on high-purity silicon crystals with resistivity about $12\,\mathrm{k\Omega}\cdot\mathrm{cm}$ and residual impurity concentration not higher than $10^{12}\,\mathrm{cm^{-3}}$. Figure 12, *a* shows the characteristic exciton THz-PL spectrum at 5 K and interband photoexcitation density $0.1\,\mathrm{W/cm^2}$.

The THz emission spectrum shows narrow emission lines with maxima at energies of 10.2, 11.4 and 12.1 meV. The spectral position and shape of these lines allows us to attribute them to optical transitions between the sublevels of 2P and 1S states of the free exciton. Similar lines were also observed in the absorption spectra of free excitons in Si [120,121]and were assigned to three groups of optical transitions between the sublevels $1S^{3/2}_{\pm3/2}$ and $1S^{3/2}_{\pm1/2}$ of the ground state of exciton and sublevels $2P^{1/2}_{\pm1/2}$, $2P^{3/2}_{\pm1/2}$,

$2P^{5/2}_{\pm 1/2}$ and $2P^{3/2}_{\pm 3/2}$, $2P^{5/2}_{\pm 3/2}$, $2P^{5/2}_{\pm 5/2}$ of excited state (see Figure 12, *b*). The broader line in the THz-PL spectrum at energy about 13.6 meV can be attributed to optical transitions from a highly excited state to the ground state of free exciton. Structureless THz PL at energies above 15 meV (Figure 12, *a*) is most likely due to emission transitions from continuum states to the ground exciton state. With temperature increasing, the lines of intraexciton emission transitions broaden and decrease in amplitude. At temperatures above 20 K intraexciton THz PL transforms into an asymmetric line with a maximum at an energy about 11.6 meV. Exciton THz emission becomes weak at temperatures above 50 K, which is associated with the excitons dissociation at high temperatures [110]. In the range of photoexcitation densities of 0.1 to 1 W/cm^2 used in the paper [110], exciton THz PL depends linearly on the photoexcitation intensity. This fact indicates that exciton THz emission can reach high intensity under intense interband photoexcitation. This significantly distinguishes exciton emission from impurity THz PL caused, for example, by D^0h-recombination [96–98], which tends to saturation with pump intensity increasing.

In high-purity silicon crystals the intraexciton emission determines the THz-PL spectrum both at low photoexcitation levels (about fractions of W/cm^2) and at high levels (THz-PL was studied at photoexcitation densities up to 140 W/cm^2 [108,109]). The condensation of excitons into EHL droplets, which occurs in silicon at high levels of interband photoexcitation [122], does not occurs in any way in the exciton THz-PL spectrum [108,109], except for the fact that under condensation conditions the temperature dependence of the THz-PL intensity becomes non-monotonic with maximum at temperatures about 10−17 K, depending on the level of photoexcitation.

It was found in papers [108,109,123] that at temperatures above 20 K exciton THz-PL becomes superlinear in pump intensity at interband photoexcitation densities above 10 W/cm^2 (see Figure 13). The threshold for the transition from linear to superlinear dependence of the exciton THz-PL intensity on the pump intensity is about 7 W/cm^2. The observed patterns (Figure 13) in the papers [108,109,123] were explained by the appearance of stimulated exciton THz emission, and, accordingly, the appearance of population inversion in the excitons system at high level of interband photoexcitation. The population inversion occurrence in excitons system appears at temperatures above 20 K is explained by the fact that at temperatures above the value critical for the EHL (about 23 K for Si [122]) the excitons condensation into EHL is absent, and, accordingly, a high concentration of free excitons is achieved under intense photoexcitation [108,109,123].

Note that the possibility of achieving population inversion between the levels of free excitons and, accordingly, laser THz generation on intraexciton optical transitions under intense interband photoexcitation of the crystal was previously theoretically predicted (see, for example, [124,125]). In the paper [126] using the method of coherent spectroscopy in

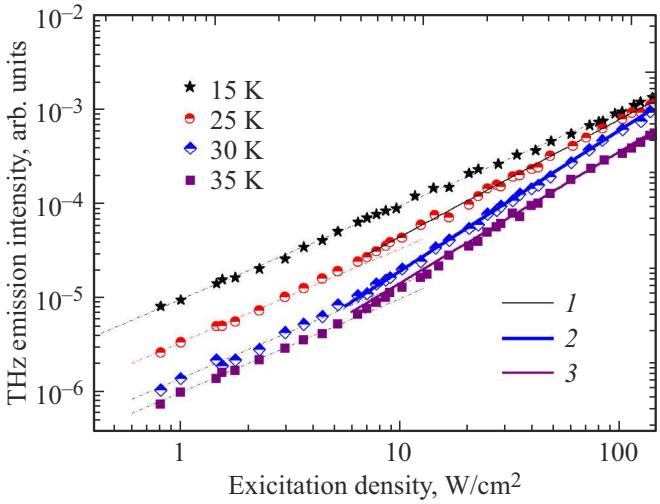

Figure 13. Spectrally integrated THz-PL intensity in high-purity silicon vs. interband photoexcitation density. Dots — experimental data, dotted lines — the result of data approximation by linear function, solid lines — results of experimental data approximation by power functions: *1* — $I_{PL} = \text{const}_1 (I_{exc})^{1.25}$, *2* — $I_{PL} = \text{const}_2 (I_{exc})^{1.5}$, *3* — $I_{PL} = \text{const}_3 (I_{exc})^{1.4}$.

the variant „optical pump — THz probe“ the appearance of intraexciton population inversion was recorded in crystals Cu_2O under intense interband photoexcitation. In these experiments, only negative absorption was directly observed at transitions between levels of free excitons, which allowed the authors of the paper [126] to conclude that population inversion between exciton levels was achieved. Stimulated THz emission caused by optical transitions between levels of free excitons with inverted population was not directly observed in the paper [126].

In papers [109,123] experiments were carried out that made it possible to confirm the appearance of stimulated intraexciton THz emission in silicon crystals at a high level of interband photoexcitation. In these experiments the pump laser radiation was focused using a cylindrical lens into a line of size 2.5×0.15 mm^2 onto the surface (111) of Si wafer having transverse dimensions 7×7 mm^2 and thickness 0.5 mm. THz emission was recorded from the side face of the sample in the direction perpendicular to the normal to the surface of the silicon wafer. A slot diaphragm with a hole length of 4 mm and a width of 0.5 mm, made from copper foil 0.1 mm thick was placed on the silicon wafer side face that is the output for THz emission. Terahertz emission was measured in the direction both along the excitation line (configuration A in Figure 14) and across (configuration B in Figure 14). Figure 14 shows the results of THz-PL measurements at photoexcitation density of 35 W/cm^2 and temperature of 25 K, that is, under conditions when the exciton THz emission is superlinear in pump intensity (see Figure 13). To analyze the results, the emission spectra were normalized to the maximum to compensate for the difference in the conditions for

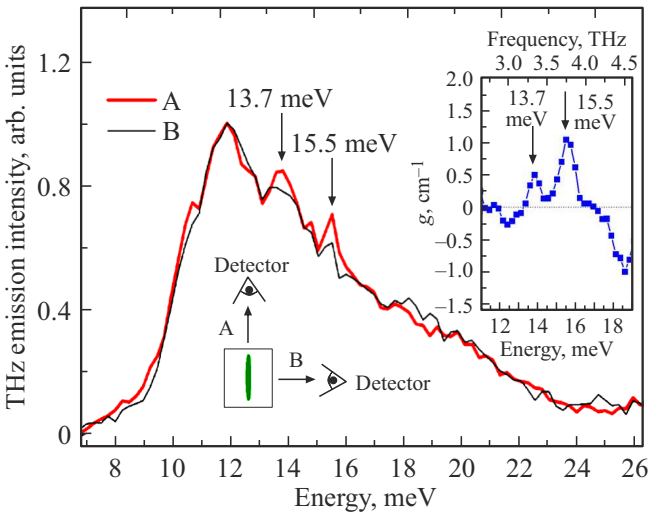

Figure 14. THz-PL spectra of high-purity silicon at interband photoexcitation density of 35 W/cm^2 and $T = 25$ K. Pump laser radiation with wavelength of 530 nm was focused into line of size 2.5×0.15 mm^2 onto the sample surface. Spectra are normalized to maximum. The insert below shows the geometry of the experiments in configurations A and B. The insert at the top shows THz spectrum of the gain obtained as a result of processing the THz-PL spectra.

collecting THz emission and delivering it to the detector in configurations A and B.

It is clear from Figure 14 that THz emission contribution on the lines at 13.7 and 15.5 meV increases noticeably in the case of recording emission along the photoexcitation line (configuration A in Figure 14). This indicates that there is THz emission amplification on these lines (amplified spontaneous emission), which, in turn, is due to the population inversion in the excitons system under experimental conditions. Data processing from such experiments made it possible to obtain THz amplification spectrum [109,123], and such a spectrum is shown in the insert of Figure 14. The spectrum shows two lines with positive THz amplification at 13.7 and 15.5 meV. Negative values of the coefficient g correspond to absorption. The gain on the 13.7 and 15.5 meV lines is about 0.5 and 1.0 cm^{-1}, respectively. The line at 13.7 meV in the THz amplification spectrum is due to the population inversion between the highly excited states of free excitons and the ground exciton state. In the paper [109] the processes of energy relaxation of free excitons with the emission of acoustic phonons in silicon crystals were considered. The results of this consideration showed the fundamental possibility of the appearance of population inversion between exciton states during the energy relaxation of excitons. The line at 15.5 meV in the THz amplification spectrum (i. e. at energy above the binding energy of free exciton in Si) is, may be, due to the population inversion between the two-exciton and biexciton states [109,123]. The possibility of the population inversion occurrence between the two-exciton and biexciton states under conditions of intense single-photon excitation of excitons from the ground state of the crystal was predicted theoretically in paper [127].

The values of the THz gain on exciton optical transitions obtained for high-purity Si crystals (Figure 14) are comparable with the gain values typical for THz laser on intracenter transitions in donor-doped Si when pumped by CO_2-laser radiation (see Section 2.2 above). Therefore, the data obtained in the papers [109,123] indicate that it is possible to create the exciton THz laser on silicon. To implement such exciton laser it is necessary to provide volumetric pump of the silicon crystal and create THz resonant cavity with low losses.

3. Classical methods for generating THz emission

Advancement into the THz region of the spectrum occurs both from the side of the light waves region and from the side of microwave radiation. In Part 2 of this review the attention was paid to the generation of THz emission caused by optical transitions between electronic energy levels in semiconductors (THz emission during quantum transitions). Methods for generating THz emission using semiconductor microwave electronic devices are also being developed. Although the operation of semiconductor devices such as a resonant tunnel diode or SL is based on quantum phenomena in solids, methods for generating THz emission using microwave technologies are not directly related to quantum transitions between electronic energy levels. Thus, these methods can be conditionally classified as classical methods for generating THz emission. For the same reason, classical methods for generating THz emission include THz generation when exciting semiconductors and semiconductor structures with ultrashort laser pulses in the visible or near-IR ranges. This part of the review relates to classical methods of generating THz emission.

3.1. Generation of THz emission using microwave technologies

3.1.1. Frequency multiplication of microwave emission

The generation of THz emission under this method is based on the use of a microwave synthesizer as a source of initial (reference) emission and a semiconductor nonlinear element, with the help of which harmonics of the frequency reference signal are generated (semiconductor frequency multiplier). In principle, this method of generating THz emission is similar to the method of generating harmonics of light waves in nonlinear optics. Microwave synthesizers based on Gunn oscillators or generators based on avalanche transit diodes can produce emission with frequencies up to the frequency about 100 GHz [4,5,128,129]. Schottky barrier diodes are traditionally used as frequency multipliers,

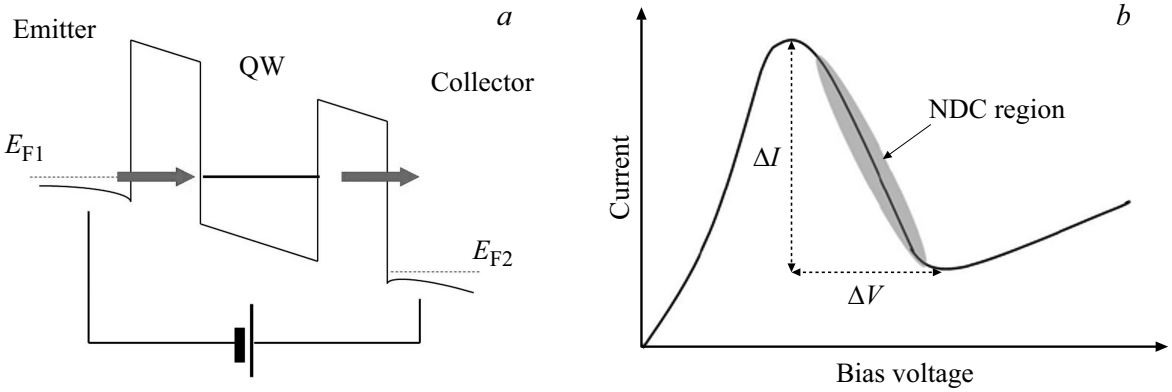

Figure 15. *a* — schematic energy band diagram of resonant double-barrier heterostructure (RTD) at bias voltage corresponding to the resonant tunneling passage of electrons from the emitter to the collector. *b* — schematic IVC of RTD structure. The maximum on IVC corresponds to the resonant tunneling of electrons from the emitter to the collector.

placed in a corresponding waveguide to output the generated emission of high-frequency harmonics [129]. The frequency of the reference signal can be multiplied sequentially in several sections to achieve higher frequencies. The main disadvantage of Schottky barrier diode based multipliers is the relatively high parasitic capacitance, which limits their use for generating harmonics at frequencies above 1 THz [130]. More promising is frequency multiplication using semiconductor SLs [130–132], which makes it possible to generate THz emission at high harmonic numbers of the reference microwave emission. The strong nonlinearity of $I-V$-charcteristic (IVC) of semiconductor SL at a certain bias voltage is due to Bragg reflections of electrons at the boundaries of SL Brillouin mini-band and momentum relaxation processes in the mini-band [11,72], and such nonlinearity persists up to frequencies about several THz. Using frequency multiplier based on GaAs|AlGaAs SL the THz spectrometer was demonstrated for the spectral region 1–2 THz for gas spectroscopy with a spectral resolution about 1 MHz [130].

THz emission sources based on microwave emission frequency multiplication operate at room temperature, but the power of the generated THz emission is quite low and decreases significantly with frequency increasing. At the output emission frequency ~ 1.7 THz, the output power of the THz emission source based on frequency multiplication in the best case is about units of μW [4], and at frequency of 5 THz the emission power does not exceed fractions of nW [132].

3.1.2. THz generation using resonant tunnel diodes

Compact THz emitters with electrical excitation operating at room temperature are also created on the basis of resonant tunnel diodes (RTDs). RTD is a two-terminal semiconductor device with a section of negative differential conductivity (NDC) in IVC [72]. The simplest version of RTD is a heterostructure with a single deep QW based on a narrow-gap material, placed between two wide-gap barriers (Figure 15, *a*). The structure also contains emitter and collector regions made of material similar to the QW material. The emitter and collector regions can be heavily doped up to degeneracy level. With bias voltage increasing the current through such heterostructure increases and reaches maximum when the position of the Fermi quasi-level in the emitter is aligned with the position of the first level of size quantization of electrons in QW (Figure 15, *a*). With a further increase in the bias voltage, the probability of electron tunneling through QW drops, and the current begins to decrease, which leads to the appearance of NDC section in the IVC of the structure (Figure 15, *b*), which is used for generation THz oscillations [133–137]. In THz emitters based on RTD, the structure of the resonant tunnel diode, together with lines for supplying bias voltage, is integrated with the antenna, which serves as a resonant cavity, and also emits electromagnetic THz wave into the ambinient space. Both patch antennas [133] and slot antennas [134], designed for the THz frequency range, are used. Figure 16 shows the equivalent circuit of THz emitter based on RTD. THz oscillations in such circuit and, accordingly, emission of electromagnetic THz waves arise in the case if the value of the NDC of RTD structure exceeds the total conductivity of the antenna, i. e. subject to condition $|G_{RTD}| > G_{Ant}$. Typically, the capacitance of the RTD structure is significantly greater than the capacitance of the antenna, and the inductance of the antenna exceeds the inductance of the RTD [134]. Therefore, the frequency of the resulting electromagnetic oscillations is actually determined by the capacitance of the RTD structure and the inductance of the antenna, i. e.

$$f_{osc} \approx \frac{1}{2\pi\sqrt{L_{Ant}C_{RTD}}}. \quad (1)$$

The best results to date in generating THz emission (in terms of generated frequencies and output power) using RTDs were achieved for heterostructures containing

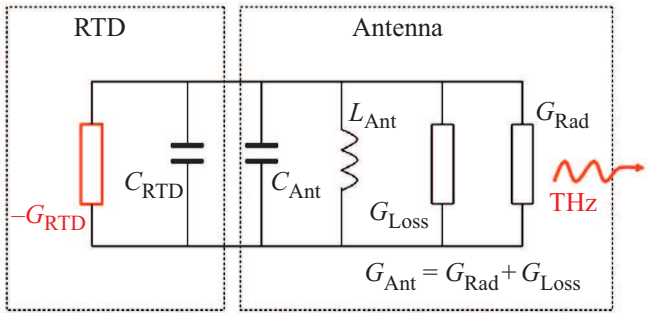

Figure 16. Simplified equivalent circuit of THz emitter based on RTD structure integrated with antenna. G_{RTD} — the value of the negative differential conductivity of the structure. G_{Ant} — equivalent conductivity of the antenna, which is the sum of conductivity of losses in the antenna G_{Loss} (ohmic losses) and conductivity G_{Rad} associated with electromagnetic waves emission. C_{Ant} — antenna capacitance, C_{RTD} — RTD structure capacitance, L_{Ant} — antenna inductance.

InGaAs quantum well between AlAs barriers grown on InP substrates. Based on heterostructures of this type, RTD THz emitters with emission frequencies of 1.92 THz [135] and 1.98 THz [136] were demonstrated.

To achieve the maximum power of THz emission, it is important to obtain the maximum possible extent of the bias voltage in the region of NDC, ΔV, as well as the maximum current peak-to-peak amplitude, ΔI, in NDC region (Figure 15, *b*), since the emission power of RTD oscillator is proportional to the product $\Delta V \cdot \Delta I$ [134]. The characteristic values of ΔV are about 0.3 V, and for ΔI about 10 mA for an RTD with an area of 0.85 μm^2 [134]. The power of THz emitter based on RTD turns out to be related to the generation frequency, since the frequency depends on the RTD structure capacitance (expression (1)), i. e. on RTD area, and the THz emission power also depends on the area (through the variable ΔI). In the general case, THz emission power for a single RTD oscillator decreases with emission frequency increasing [134,137]. For THz emitter based on RTD with THz generation frequency 0.517 THz the emission power about 10 μW was obtained [133]. Optimization of RTD structures and antenna parameters made it possible to obtain the first RTD oscillators generating emission at frequencies about 1 THz and higher with emission power of 20 μW at 1 THz and 1 μW at 1.4 THz (see [134]). The paper [137] presents the study results of a number of RTD oscillators with different frequencies of 1.06 to 1.75 THz, THz emission power at 300 K for which ranged from 0.97 μW at frequency 1.06 THz to 0.1 μW at 1.75 THz. In the same paper the properties of THz emitters based on RTDs were studied in the temperature range 4.2–300 K. It was shown that the frequency of THz generation in RTD oscillator is practically independent of temperature. However, the power of THz emission decreases significantly with temperature increasing, which is explained by increase in ohmic losses in the antenna electrodes [137].

The emission spectrum of THz emitter based on separate RTD oscillator contains a single narrow line, the spectral width of which, unless special measures are taken to achieve ultra-narrow emission line, can be about 10 MHz [138]. To narrow the spectral width of the emission line, more complex designs of THz emitters based on RTDs are used, in which the RTD oscillator is integrated with a varactor diode (a diode used as variable capacitance) and is connected in the loop with negative feedback, providing phase-lock [134]. For such THz emitters the emission linewidth about 1 Hz [139] was demonstrated. For single RTD THz emitters integrated with varactor diodes, the possibility of tuning the generation frequency by about 100 GHz [140] was demonstrated.

It was theoretically shown that by optimizing the structure of the resonant tunnel diode, its interfacing with resonator cavity in the form of a cylindrical cell and antenna of „bow tie“ type for single RTD in form of RTD oscillator, THz generation with frequency of up to 2.8 THz and emission power about 1 μW can be achieved [141].

An interesting result was obtained for an array of frequency-tunable RTD emitters, also integrated with varactor diodes and having different frequency tuning ranges[142,143]. For such array of THz emitters, tuning of the frequency of THz emission in the region of 410–970 GHz was achieved, which makes it possible to use such combined semiconductor THz source, for example, for absorption spectroscopy of various media [143]. The use of arrays of emitters based on RTDs also makes it possible to significantly increase the power of THz emission. In a two-dimensional array of RTD emitters containing 89 individual elements, between which there was no phase synchronization, THz emission power about 0.7 mW [144] was obtained. The emission spectrum in this case contained several overlapping lines in the region of 1.0–1.05 THz with the maximal intense line at frequency about 1 THz [144]. In the array of RTD emitters consisting of two elements, between which phase synchronism was achieved, and coherent summation of the amplitudes of the THz fields of the emitters occurred, a single THz generation line was obtained with frequency of 0.62 THz and emission power about 0.6 mW [145].

Such properties of THz emitters based on RTDs, as their compactness, moderate level of emission power, narrow THz generation line, high stability of the generation frequency, relatively simple methods of THz emission modulation (both amplitude and frequency [134]) make THz sources of this type promising for numerous applications. Among such applications are — THz visualisation of various objects [146], THz spectroscopy [143], THz sensors [147], emitters for data transmission systems at THz frequencies [148], as well as THZ radars [134].

3.1.3. THz emitters based on high-frequency transistor circuits

It is well known from radio engineering that a high-frequency amplifier, built, for example, on bipolar or field-effect transistors, with positive frequency-dependent feedback, becomes a generator of high-frequency electrical oscillations. To date, significant progress was made in the creation of THz emitters operating at room temperature based on heterojunction bipolar transistors (HBTs), field-effect transistors with a high electron mobility channel (HEMT), as well as complementary transistors of metal-insulator–semiconductor type (CMOS) [149–156].

In paper [149] 35 nm HEMT technology was used to create THz emitters based on InP. The authors used a HEMT structure obtained by the MBE method with $In_{0.75}Ga_{0.35}As$ channel with electron mobility about $1.2 \cdot 10^4$ cm^2/Vs and concentrations $3.5 \cdot 10^{12}$ cm^{-2}. The T-shaped gate of the field-effect transistor had an active width about 35 nm. The used 35-nm technology made it possible to obtain maximum frequency $f_{\max}$ of transistor amplification about 600 GHz [149]. Fundamental oscillators with generation frequencies of 0.254, 0.314 and 0.346 THz were created, which are integrated circuits (ICs) that contain the transistor itself, coplanar waveguides, which also act as a resonator cavity and feedback element, as well as matching circuits. The total size of the integrated circuit was 0.4×0.4 mm^2. THz generation powers were 158, 46 and 25 μW at frequencies 0.254, 0.314 and 0.346 THz, respectively [149]. The THz generation linewidth was about 1 MHz.

Based on 65-nm technology of silicon CMOS transistor, ICs of frequency-tunable THz emitters with high output power were designed and created in paper [150]. ICs contained several external voltage-controlled coupled oscillators. The integrated circuit provided generation, summation of emission from coupled oscillators, and output of THz emission to the output port of IC. For an emitter of this type with a generation frequency of 0.29 THz, output emission power about 0.76 mW was obtained, and the tuning range of the generation frequency reached 13 GHz. For emitter with generation frequency of 0.32 THz, the output emission power and the tuning range of the generation frequency were about 0.46 mW and 8.4 GHz, respectively [150].

The paper [151] demonstrated THz emitter based on SiGe IC created using 130 nm BiCMOS technology (technology combining elements of HBT and CMOS technologies), with a center emission frequency 0.53 THz, frequency tuning range up to 17 GHz and THz emission output power about 1 mW. The IC is a matrix of 16 individual THz emitters (pixels) with integrated ring antennas. The emitting pixels were not coherent with each other. This THz emitter was designed specially for applications in THz visualisation of various objects. Feature of SiGe THz emitters based on HBT and used in [151] is that the transistors initially generate at frequency f_0 about 175 GHz. Due to the nonlinearity in the SiGe transistor in the strong signal mode [151] odd frequency harmonics f_0 are also generated, of which the third one (525 GHz) is the strongest. The frequency 525 GHz is separated in IC and supplied to the emitting antenna. The THz emitter module created in [151] had the ability to be programmed (via a USB port) to control both the direction of emission propagation and its intensity. The module size was 2.0×2.1 mm^2. According to measurement data [151] the width of the emission pattern at half power was $\pm 15^\circ$. The authors [151] emphasize that the developed design of the THz emitter IC is scalable both in terms of the IC size, and the power of the output THz emission.

Using 130-nm BiCMOS technology, SiGe-THz emitter with a generation frequency of 1 THz based on a matrix of 42 (6×7) emitters coherent with each other (phase synchronized) was developed and created in paper [152]. The size of individual emitter (cell) in the matrix, including two slot antennas (vertical and horizontal) per emitter [152], was about $\lambda/2$ (where λ — emission wavelength at frequency 1 THz). The total power of THz emission reached 80 μW, and the width of the emission pattern at half power was about $\pm 5.5^\circ$ in both the vertical and horizontal planes. Since the maximum power amplification frequency, $f_{\max}$, for heterojunction bipolar SiGe transistors does not exceed 0.5 THz [153], in paper [152], as in [151] the method of active frequency multiplication was applied. In the transistor circuits of individual emitters the frequency $f_0 = 250$ GHz and its harmonics $2f_0$, $3f_0$ and $4f_0$ were first generated. In this case, the first, the second and the third harmonics are suppressed in the emitter circuits, and the fourth harmonic with frequency of 1 THz is supplied to the emitting antennas. The total size of the THz emitter IC is 1×1 mm^2. According to the authors [152], the developed design of IC of coherent THz emitter can also be scaled to increase the emission power.

For transistor amplification circuits HBTs based on InP, maximum signal power amplification frequencies $f_{\max}$ exceeding 1 THz (frequency of 1.15 THz [154] was actually demonstrated) were achieved. Unprecedented frequency band for InP HBTs was achieved due to a combination of several factors, including the properties of the InGaAs|InP material system (high electron mobility in *p*-base of the transistor, a large discontinuity in the conduction band at the heterojunction, the ability to achieve high level of layers doping, which makes it possible to obtain low-resistance ohmic contacts), as well as scaling the lateral and vertical dimensions of transistors to the nanometer region [155,156]. Such high operating frequencies of HBTs InP made it possible to create terahertz monolithic ICs (TMIC) based on them, the most important blocks of which include amplifiers, fundamental oscillators with external voltage control, local oscillators for heterodyne signal reception circuits, mixers, frequency dividers, phase shift circuits. phase-locked loops, etc. [155,156]. Such TMIC can be used in compact devices for THz probing and visualization of various objects, for THz radars, and also for THz communications equipment.

Using 250-nm HBTs InP technology, ICs of THz emitters tunable by external voltage with a generation frequency in the region of 0.57 THz, emission power about 10 μW, and range of generation frequency tuning about 10 GHz were created [155]. The emission linewidth was about 1 MHz. The transition to 130-nm HBTs InP technology made it possible to create THz emitter ICs with frequencies up to 0.688 THz [156]. THz emission power for such emitters was $1-3\,\mu$W. In the paper [156] it was noted that mutual integration of InP HBT and Si CMOS elements into one integrated circuit is possible, which will significantly increase TMIC functionality.

THz emission emitters built using HBT, HEMT, CMOS technologies of transistor IC are promising for various practical applications, such as THz emitters based on RTD technologies. In terms of the level of generated THz power, the transistor emitters are comparable to emitters based on RTDs. However, the achieved THz generation frequencies for RTD emitters are noticeably higher compared to the frequencies achieved in transistor emitters (Section 3.1.2), and may in the future reach frequencies about 3 THz (see, for example, [141]).

3.2. THz generation using the ultrashort laser pulses technology

It is well known that when many materials are excited by femtosecond laser pulses, pulses of electromagnetic emission of subpicosecond duration are generated, the frequencies of which lie in the terahertz region of the spectrum [1,3–5]. Note that the ideas about the energy conversion of ultrashort laser pulses into coherent emission in the THz range in nonlinear crystals due to the difference frequency generation effect (or the effect of optical rectification of laser pulses with broadened frequency spectrum) were theoretically formulated back in the 1970s. (see, for example, [157]). In mid-1980s with the appearance of the first femtosecond lasers, a group headed by D.H. Auston obtained experimental results confirming the possibility of converting the energy of ultrashort laser pulses into THz emission in nonlinear crystals. The same group of authors demonstrated the generation of short pulses of THz emission during femtosecond laser photoexcitation of semiconductor photoconductive antenna based on radiation-damaged Si on sapphire (RD-SOS).

To date, the generation of THz emission pulses containing several cycles of electromagnetic oscillations was observed in dielectric crystals, semiconductors, metals, and even in gases and liquids (see, for example, [4,5], [160] and other references there). In general, such THz generation mechanism is associated with excitation in the material or structure of a fast dipole or short photocurrent burst [4,5]. Using Maxwell's equations, it can be shown [5,161] that in far field the amplitude of the generated electromagnetic THz wave, E_{THz}, is proportional to $\partial^2 P/\partial t^2$ or $\partial J/\partial t$, where $P(t)$ and $J(t)$ are, respectively, the time-varying dipole moment or current induced by the exciting laser radiation. The coherent THz emission generated in this way found application in THz spectroscopy (THz-TDS) and THz visualisation of various objects. The undoubted advantage of THz-TDS technique is that all the main components of the measuring system, both the source and the receiver of THz emission (note that the receiver is also coherent, is gated by femtosecond laser pulses and measures the field amplitude of the electromagnetic THz wave — see, for example, [161]), operate at room temperature, and the signal-to-noise ratio in terms of signal amplitude in the measuring system can reach 10^4 and even more (and at least 10^8 in power) [162,163]. Details of the organization of THz-TDS measuring systems, features of such system components and THz signals processing can be found, for example, in [164].

Efficient generation of coherent THz emission under femtosecond laser photoexcitation is realized in bulk semiconductors and semiconductor structures. This Section of the review examines such THz generation schemes.

3.2.1. Generation of THz emission in photoconductive antennas

Among semiconductor emitters excited by femtosecond laser radiation, in terms of practical use, THz emitters based on photoconductive antennas with external bias are the most popular. The operation of THz source based on photoconductive antenna (PCA) is illustrated in Figure 17. The emission pulse of femtosecond laser (for example, a titanium-sapphire laser with characteristic wavelength of 800 nm, generating pulses with width about $10-100$ fs with repetition rate about 80 MHz) is focused in the gap between two electrodes deposited on the surface of semiconductor (photoconductor), the band gap of which is less than the energy of the pump laser quantum. A constant voltage is applied between the electrodes. Electrons and holes generated by light are accelerated in the electric field created between the electrodes, and are also captured by impurities and crystal defects with subsequent recombination, which results in a short burst of photoconductivity current in the circuit. A material with short lifetime (in the subpicosecond time range) and high mobility of non-equilibrium charge carriers is used as a photoconductor. Besides, the photoconductor material should have a high voltage (field strength) of electrical breakdown. The material that meets these requirements is gallium arsenide, grown by the MBE method under conditions of low temperatures (about 200°C) — so-called. low temperature GaAs (LT-GaAs) [165]. The LT-GaAs layer without illumination has a low equilibrium conductivity, and therefore the dark current in PCA based on it is small, which makes it possible to use rather high bias field strengths in such PCAs (from several kV/cm to values about 100–120 kV/cm [166]).

Thus, the femtosecond laser pulse creates in the gap between PCA electrodes a short burst of photocurrent $J_{\mathrm{Ph}}(t)$(Figure 17, *b*), which, like Hertz dipole, emits a pulse

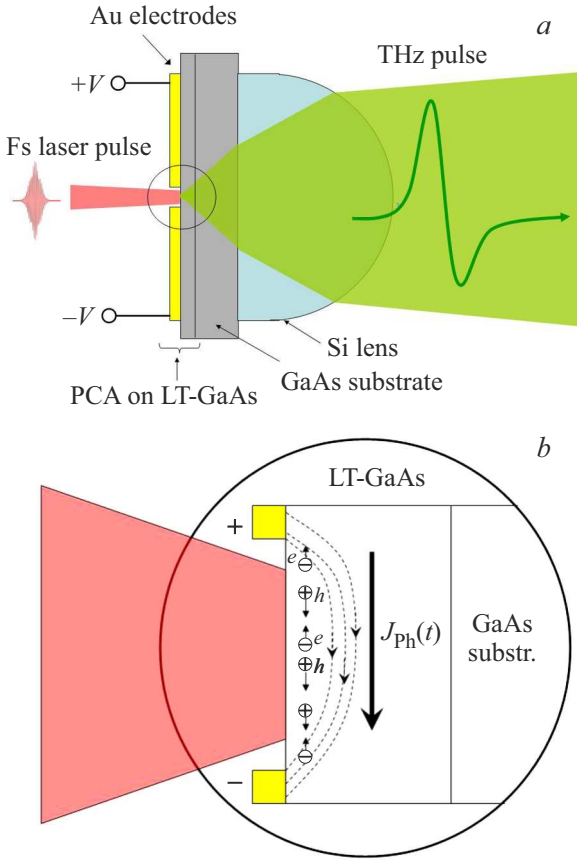

Figure 17. *a* — schematic representation of THz emission source based on dipole PCA. The PCA electrodes can be made, for example, in the form of „bow tie" antenna, and the PCA can be integrated with a hemispherical or super-hemispherical silicon lens for collimation of the THz emission beam. *b* — Enlarged image of the photoexcitation region of PCA. Generation of non-equilibrium electron-hole pairs and fast photocurrent $J_{Ph}(t)$ in the gap between the electrodes.

of THz emission containing several cycles of electromagnetic oscillations [5]. As noted above, in the far field (in the wave zone) the amplitude of the electric field of the emitted THz wave is proportional to the first derivative $J_{Ph}(t)$ with respect to time. Broadband THz emission is generated, the spectrum width of which is largely determined by the duration of the photocurrent pulse.

Depending on the ratio between the size of the photoexcitation region in PCA and the wavelength of the generated THz emission, dipole and wide-aperture PCAs are distinguished. In dipole PCAs the size of the illumination region is significantly smaller than the wavelength of THz emission (Figure 17 corresponds to dipole PCA). Dipole PCAs are suitable as simple THz emitters in THz-TDS measuring systems based on femtosecond lasers with high repetition rate and relatively low peak power. The design of the electrodes in the PCA and their shape play an important role in the transfer into the wave zone of both high frequencies of the THz electromagnetic field generated near the gap between the electrodes and the power of THz emission. The following designs of simple dipole photoconductive antennas are used: „strip line", „Hertz dipole"„offset dipole", „bow tie" (Figure 18, *a*–*c* and *d* respectively) [167–170]. In PCA with strip line design of electrodes the shorter pulses of THz emission are achieved than in PCA, for example, with electrodes of Hertz dipole type, and, accordingly, PCA with strip lines generate THz emission with wider spectrum, but the emission power for strip PCAs is lower.

The average power level of THz emission generated in simple dipole PCAs demonstrated in the early 1990s was about 10–40 nW [171,172]. The efficiency of THz generation in PCAs can be significantly increased by optimizing the structure of the electrodes. In the paper [169] the pointed and shifted relative to each other electrodes were used in PCA based on LT-GaAs (Figure 18, *c*). In such PCA at a bias voltage of 60 V and average power of the femtosecond pump laser of 20 mW, the average THz emission power about 3 μW was achieved, which corresponds to peak power per pulse about 30 mW. The spectrum of the generated THz emission extended to frequency about 2.3 THz [169]. In THz beam focused to a size about 0.5 mm, the THz electric field strength about 57 V/cm was obtained.

Using photoconductive antennas based on LT-GaAs, generation of THz emission with frequencies up to 15 THz [173] was obtained. In this paper, the dipole PCA with electrodes in the form of strip line was used. A titanium-sapphire laser with pulse width about 12 fs was used as a source of photoexcitation, and PCA was also used as THz detector (the PCA operation in THz detector mode was considered, for example, in [5,161,164]). Despite the dip in the spectrum of THz emission in the frequency range between 8.0 and 8.8 THz, due to absorption by optical phonons in GaAs, such THz emitter (as well as emitter-detector pair) can be used for broadband THz spectroscopy.

Note that in the paper [174] the efficient THz emitter based on dipole PCA was demonstrated, it was developed for applications in THz-TDS systems using the femtosecond pump laser with wavelength of 1550 nm. The material for such PCA was InGaAs solid solution doped with rhodium, obtained by MBE method on a semi-insulating InP substrate. At bias field strength between PCA electrodes of 60 kV/cm (the distance between the electrodes was about 25 μm) and average pump laser power of 28 mW, an average THz emission power of 637 μW was achieved [174].

The field strength of the THz emission generated in PCA increases with bias voltage growth according to law close to linear one [5,161]. At low bias voltages the THz emission field strength also increases with photoexcitation power increasing, but only up to certain photoexcitation power levels, which depend on the design of the PCA electrodes. At high levels of photoexcitation the dependence of THz field strength on the pump power reaches saturation [5,161]. In PCA with „bow-tie" electrodes (Figure 18, *d*), saturation of

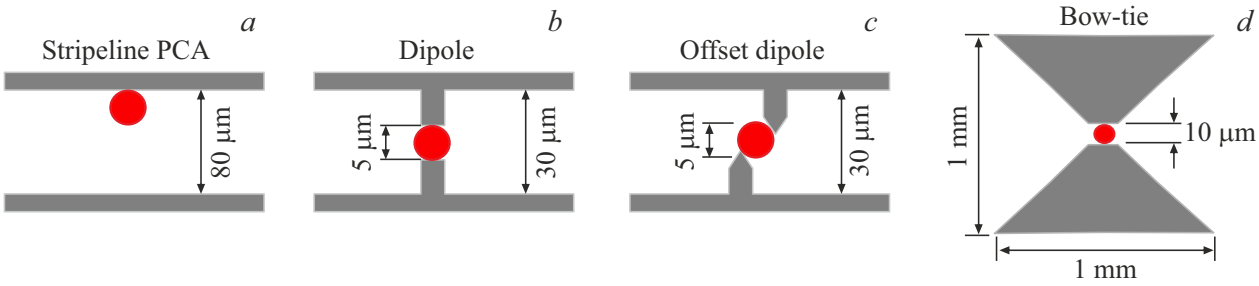

Figure 18. Schematic diagrams of dipole PCAs with different designs of electrodes: *a* — „strip line“, *b* — „Hertz dipole“, *c* — „offset dipole“, *d* — „bow tie“. The red-shaded circle corresponds to the photoexcitation spot.

THz field amplitude appears at higher photoexcitation levels compared to PCA with another design electrodes [161].

The effect of amplitude saturation of THz emission field in PCA with increase in photoexcitation power is explained by the occurrence of the electric field screening in the gap between the electrodes by non-equilibrium electrons and holes generated by the pump laser (polarization screening or space charge effect), as well as by the occurrence of the so-called emission screening associated with the inductive response of PCA to the emitted THz field [5,161]. This inductive reaction is due to partial compensation of the electric bias field of PCA by the field of the generated THz wave [175]. It was shown in the paper [176] that the effect of saturation of interband absorption (bleaching effect) in the PCA material at high level of photoexcitation also contributes to the saturation of the field amplitude of the generated THz emission observed in PCA with pumping power increasing.

In wide-aperture PCAs the size of the photoexcitation region significantly exceeds THz emission wavelength. Such PCAs are convenient for generating THz emission pulses with high peak power when photoexcited by the radiation of femtosecond lasers with regenerative amplifiers, i. e., lasers with high output pulse energy and low repetition rate [161,166]. The gap between the electrodes in such PCAs ranges from 0.5 mm to several cm. The mechanism of saturation of THz emission field amplitude with pumping intensity increasing, caused by polarization screening (see above) of the electric bias field, which is essential for dipole PCAs, does not have a noticeable effect in the case of wide-aperture PCAs, which contributes to the achievement of high power of THz emission in such PCAs [161,166]. Saturation of THz field amplitude, associated with emission screening, as well as with saturation of interband absorption, occurs for wide-aperture PCAs[166,176].

In paper [177] in wide-aperture PCA based on LT-GaAs with size $3.5 \times 3.5\,\mathrm{cm}^2$, THz emission pulses with energy about $0.8\,\mu\mathrm{J}$ were generated at interband photoexcitation density in pulse about $40\,\mu\mathrm{J/cm}^2$ and bias field strength 10.7 kV/cm (PCA pulsed power supply was used). PCA was excited by laser pulses with wavelength of 770 nm, duration of 120 fs, and repetition rate of 10 Hz. The energy of THz emission pulses obtained in [177] corresponds to peak emission power about 1.6 MW, and in the focused THz beam the achieved amplitude of the electric field of THz wave was about 150 kV/cm. The spectrum of the generated THz emission extended to frequency about 1.5 THz. The efficiency of the optical power conversion into THz emission power, achieved for wide-aperture PCA in the paper [177], is about $2 \cdot 10^{-3}$, and the achieved THz electric field strength remains among the highest for THz emission sources based on PCA even today [166]. The high field strength of THz waves generated in such PCAs makes it possible to use THz sources of this type for studies in the field of nonlinear THz optics of various media [177].

Works on improving THz emitters based on PCAs, aimed at increasing the generation efficiency and expanding the spectrum of generated emission,are currently ongoing [166,178].

Photoconductive PCA antennas with interdigital electrodes were developed and created [166] — IDPCA. The use of interdigital electrodes makes it possible to reduce the size of the photoconductive region between individual electrodes and thus provide higher electric bias field at lower applied voltage. This increases PCA reliability and ensures their easy use. Besides, interdigital electrodes make it possible to increase the efficiency of collection of non-equilibrium carriers in PCA and, accordingly, increase the efficiency of THz generation. Such photoconductive antennas can also be called large-area PCAs. Note that THz emitters based on IDPCA were successfully commercialized (see, for example, [179]). IDPCA can be considered as an array (matrix) of individual PCAs connected in parallel. In order to sum up THz fields from such individual PCAs, the photoexcitation disabling of adjacent sections of PCA with the opposite direction of the bias field is designed (sections with only positive or only negative direction of the bias field remain open). The latter is achieved using special masks or microlens matrices [166]. In the work [180] disabling of THz emission from adjacent PCA sections with opposite directions of the bias field was achieved by complete etching such regions of the photoconductor based on LT-GaAs thin layer, transferred to insulating substrate, followed by applying interdigital electrodes system to the structure. With the help of this technology, the achievement of intense THz emission from IDPCA with THz electric

field strength about 120 kV/cm [180] was demonstrated. In IDPCA obtained using microelectronics technologies, based on semi-insulating GaAs with distance between electrodes 2 μm, generation of THz pulses with spectrum extending to frequencies about 20 THz was achieved [181]. Such a high upper limiting frequency of THz emission generated in such PCA was obtained at the cost of relatively low amplitude of the THz field due to the strong influence of the polarization screening effect of the bias field [181].

Impressive results were obtained using nanotechnology during PCA formation. Efficient THz emitters based on PCAs with nanometer-sized gaps in the comb of metal electrodes — PCAs with plasmonic electrodes were demonstrated [182]. In PCA with plasmonic electrodes based on semi-insulating GaAs, THz generation was achieved with efficiency of conversion of pump laser radiation into THz emission about 1.6% [182] (at average pump laser power of 240 mW the average power of the generated THz emission was about 3.8 mW, and the spectrum of THz emission extended from 0.1 to 5 THz). In LT-GaAs-based PCA with three-dimensional plasmonic electrodes (also having nanometer characteristic dimensions), THz generation was obtained with currently unprecedented conversion efficiency of exciting laser radiation into THz emission, amounting to about 7.5% [183].

3.2.2. THz generation with optical rectification

THz emission is also generated in nonlinear optical crystals when they interact with intense femtosecond laser radiation. The most powerful effect responsible for THz generation in such materials is the optical rectification (OR) effect, which actually is the effect of difference frequencies generation between the components of the broadened spectrum of an ultrashort laser pulse [5]. OR is a 2nd order nonlinear optical effect, determined by nonlinear susceptibility $\chi^{(2)}$ and occurs only in crystals without an inversion center. Among the semiconductors in which THz generation due to the OR effect has been studied, one can note ZnTe, InP, GaAs, GaSe crystals, etc. (see, for example, [5,184–189], as well as other references there). OR occurs both in the transparency region of crystal and in the region of interband light absorption. Omitting the vector and tensor indices, and also neglecting the dependence $\chi^{(2)}$ on frequency, the nonlinear polarization of the crystal created by ultrashort optical pulse due to OR can be expressed in frequency domain in the SI system as follows [5]:

$$P(\omega) = \varepsilon_0 \chi^{(2)} \int_{-\infty}^{+\infty} E(\omega') E^*(\omega' - \omega) d\omega', \qquad (2)$$

where $E(\omega)$ — the complex amplitude of the electric field of the light wave. The Fourier transform of equation (2) gives the value of the nonlinear polarization vector of the crystal in time domain:

$$P(t) = \varepsilon_0 \chi^{(2)} E(t) E^*(t) \propto \chi^{(2)} I(t), \qquad (3)$$

where $I(t)$ — light intensity (shape of pump pulse). Thus, the nonlinear polarization of the crystal induced due to the OR effect P completely repeats the shape of laser pump pulse, i.e. is inertia-free. The latter is very important from the point of view of generating THz emission with wide spectrum [5,161]. Therefore, OR effect in semiconductors is used to generate broadband THz emission, despite its lower efficiency compared, for example, with the efficiency of THz generation in PCAs.

The fast dipole moment Pemits THz electromagnetic wave, the electric field strength of which in the wave zone is proportional to the second time derivative of P, and the direction of THz wave field is parallel to the vector P. A more strict expression in comparison with (2) for the vector of crystal nonlinear polarization caused by the OR effect has the form [5]:

$$P_i(\Omega) = \varepsilon_0 \sum_{j,k} \chi^{(2)}_{ijk}(\Omega = \omega_1 - \omega_2) \times \int_{-\infty}^{+\infty} E_j(\omega_1 = \omega_2 + \Omega) E_k^*(\omega_2) d\omega_2, \qquad (4)$$

where ω_1 and ω_2 — frequencies of individual components in the emission spectrum of ultrashort laser pulse, and $\Omega = \omega_1 - \omega_2$ — THz frequency. In crystals of Td symmetry, which include semiconductors ZnTe, CdTe, InP, GaP, InP and GaAs, the tensor $\chi^{(2)}_{ijk}$ has only one linearly independent component ($\chi^{(2)}_{i,i+1,i+2} = \chi^{(2)}_{i,i+2,i+1} = \beta$, where i takes the values x, y or z). The symmetry of these crystals makes it possible to use the OR effect in them for THz generation in geometry per-pass, i.e. at collinear propagation of pump waves and generated THz emission.

As the pump wave and THz wave generated by OR propagate in the crystal, due to the difference in their propagation speeds a phase mismatch between these waves develops, which at large phase difference leads to destructive interference of THz fields generated from different regions of the crystal, and, accordingly, to decrease in THz emission intensity. The characteristic length of the crystal, at which the conversion of the pump wave to THz wave occurs effectively, is called the effective interaction length or coherence length, L_C [161]:

$$L_C = \frac{c}{2\nu_{THz}|n_{opt} - n_{THz}|}, \qquad (5)$$

where c — the light speed, ν — THz wave frequency, and n_{opt} and n_{THz} are refractive indices of the crystal at optical and THz frequencies, respectively. Under conditions of phase synchronism (PS) (at $n_{opt} = n_{THz}$), the value L_C becomes infinite. In this case, the intensity of the generated THz wave increases as the pump wave passes

through the crystal. Under PS conditions the amplitude of the THz wave field is directly proportional to the wave propagation length in the material [161]. At frequency of 2 THz for semiconductor crystals such as ZnTe, CdTe, GaP, InP and GaAs, PS conditions are achieved at pump wavelengths equal to 0.8, 0.97, 1.0, 1.22 and 1.35 μm respectively [161]. ZnTe crystal, therefore, according to PS conditions is suitable as THz emitter based on the effect of optical rectification during excitation by radiation from titanium-sapphire femtosecond laser with wavelength of 800 nm. Taking into account the actual width and shape of THz emission spectrum generated in ZnTe crystals, the average value of L_C is approximately 2 mm [161]. Therefore, in typical THz-TDS systems that use ZnTe-based THz emitter operating in the spectral region from 0.1–0.2 to 2.5–3.0 THz, crystals with thickness about 1 mm are used [4,5,161]. In more broadband THz-TDS systems ZnTe crystals of significantly smaller thickness are used.

In the paper [189] comparative studies of efficiency of THz generation due to OR effect in a number of semiconductor crystals (GaAs, InP, ZnTe, CdTe and GaP) were carried out. For excitation the pulses of a titanium-sapphire femtosecond laser with wavelength of 800 nm and duration of about 12 fs with average power of about 500 mW were used. It was shown that ZnTe is the best of the studied emitters for THz emission generation (both in terms of signal amplitude and maximum frequency in the spectrum) in the frequency band from 0.1 to 35 THz. Such emitter is suitable for use in broadband THz spectroscopy, despite a strong dip in the spectrum near 5.3 THz associated with absorption by optical phonons, as well as dip in the frequency region about 16.9–21.7 THz, due to the absence in this frequency region of the phase synchronism of pump waves and THz emission waves [189]. Paper [190] demonstrated the generation of THz emission due to OR effect in GaAs with frequencies up to 37 THz. Dips associated with absorption by optical phonons and the lack of phase synchronism were also observed in the THz spectrum. Interesting results on THz generation due to OR effect under phase synchronism conditions in GaSe crystals were obtained in the paper [191]. Phase synchronism in these crystals occurs in the region between 14 and 50 THz and is associated with strong birefringence in GaSe [161,191]. Paper [191] demonstrated frequency-tunable THz emission with central frequencies from 15 to 42 THz by changing the phase synchronism conditions, which was achieved by the crystal rotation.

3.2.3. THz generation upon photoexcitation of semiconductors surface

Since early 1990s it is known that excitation of the semiconductor surface by femtosecond laser pulses with quantum energy greater than the band gap of the material leads to the generation of coherent THz emission. THz generation of this type was observed at room temperature in a number of semiconductors (GaAs, InP, $Ga_{1-x}Al_xAs$ ($x < 0.2$), GaSb, InSb, CdTe, CdSe and Ge) under photoexcitation by laser radiation with quantum energy of 2 eV [192]. The papers that followed the first publication [192] on „surface“ THz generation (STG) [193–198] were aimed at studying the efficiency of THz generation and examination the effect mechanisms. It was found that THz emission comes from the near-surface region of the semiconductor, the size of which is determined by the penetration depth of the exciting light. THz emission is generated by oblique incidence of pump emission on the surface and propagates both into the bulk of the semiconductor and into vacuum (in air). Moreover, in a vacuum the generated THz emission propagates mainly in the direction of the pump laser beam reflected from the surface. Therefore, studies of THz emission associated with surface are carried out in most cases in reflection geometry, i. e. with oblique incidence of the pump laser beam at an angle of 45° relative to the normal to the semiconductor surface and detection of THz emission in the direction of mirror reflection of the exciting laser radiation [5].

STG for most semiconductors is weaker in efficiency compared to THz generation in PCA or due to the OR effect under phase synchronism conditions [5]. However, InAs crystals [199–202] are distinguished by their high efficiency of THz generation upon surface excitation. It was found that the efficiency of THz generation from InAs surface increases significantly in external magnetic field. In a magnetic field of strength 1 T for InAs crystals, the average power of THz emission about 50 μW was achieved with average femtosecond pump laser power of 1 W (titanium-sapphire laser with pulse duration 70 fs, repetition rate 80 MHz and emission wavelength 800 nm was used) [5,199]. Due to their simplicity and high efficiency „surface“ THz emitters based on InAs are extremely popular and are currently widely used in THz spectroscopy and THz visualisation systems for various objects (see, for example, [162,203], where rather efficient THz emitters based on *n*-InAs layers grown by MBE method on GaAs substrates were used, the efficiency of them is comparable to PCA).

As a result of numerous studies it was established that in the general case two effects can be responsible for STG in semiconductors [5]: 1) the effect of optical rectification of pump laser radiation in the crystal region, the size of which is determined by the light penetration depth, and 2) a short burst of the photocurrent of non-equilibrium charge carriers in the near-surface region of the crystal, directed along the normal to the crystal surface. Moreover, the latter mechanism can be contributed by both fast drift photocurrent caused by the existence of near-surface electric field [204] (or, in other words, by the bending of energy bands at the crystal-vacuum interface, see Figure 19), as well as the Dember photocurrent associated with the difference in the diffusion fluxes of non-equilibrium electrons and holes (see Figure 20).

STG due to the OR effect associated with second-order nonlinear susceptibility $\chi^{(2)}$ (Section 3.2.2) occurs only in crystals without the inversion center, and the efficiency

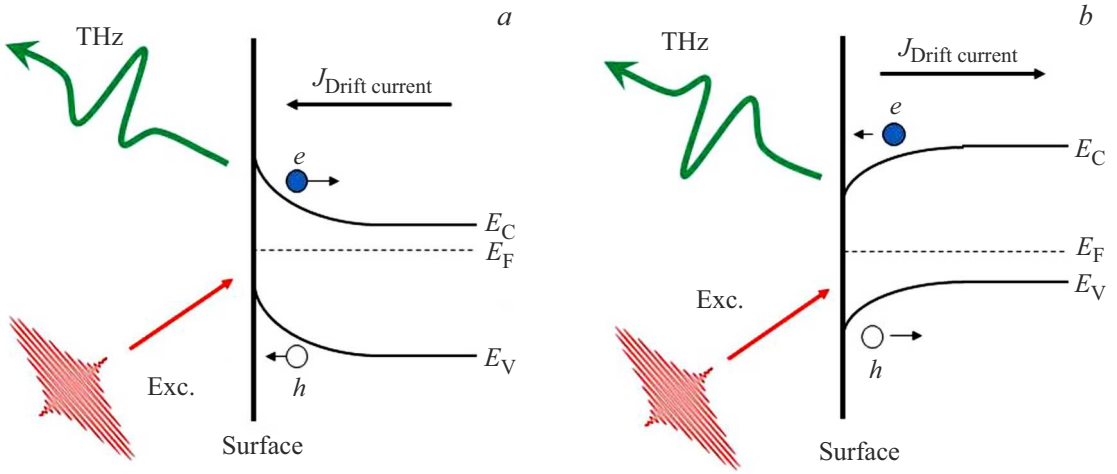

Figure 19. Schematic diagram of energy bands of crystal near crystal-vacuum interface and diagram of the THz emission formation due to ultrafast excitation and relaxation of drift photocurrent in near-surface electric field in case of semiconductor of *n*- (*a*) and *p*-type (*b*). The bands bending is caused by pinning of the Fermi level on the crystal surface [204]. The band bending is shown for GaAs-type semiconductor, for which it is known that surface states „tie" the Fermi level on the surface approximately in the middle of the band gap [204]. It can be seen that the direction of the drift current, and hence the polarity of the generated THz emission pulses will be different in the case of *n*- and *p*-type semiconductors.

of such THz generation strongly depends on the crystal orientation and polarization of pump radiation. This, in principle, makes it possible to separate the contributions to the STG from the OR effect and from the effect of excitation of the near-surface photocurrent. Analysis carried out in the paper [5] for the case of crystals with Td symmetry (InAs, GaAs, InP, InSb, etc.) in the geometry of oblique incidence of pump laser radiation at angle 45°, shows that for the crystal orientation (100) the efficiency of STG due to OR is almost by order of magnitude weaker than in the case of the crystal orientation (111). So, the crystal orientation (100) is convenient for a separate study of the contribution to the STG due to the excitation of the near-surface photocurrent. For InAs crystals with the orientation (111), in which both contributions to the STG are significant, it was shown [5] that the amplitude signal of STG due to the OR effect is no more than 40% of the total THz signal. Note that along with the OR effect caused by the second-order nonlinear susceptibility $\chi^{(2)}$, it is possible to observe OR associated with the third-order nonlinear susceptibility $\chi^{(3)}$ [186–188,205] and caused by electric field-induced optical rectification (EFI OR) [206]. THz generation due to the EFI OR effect also has a strong dependence on the crystal orientation and the pump emission polarization.

Experimental data on STG obtained on InP and GaAs crystals with the orientation (100) show that THz generation prevails in these materials due to fast photocurrent in near-surface electric field [5]. In narrow-gap InAs and InSb crystals, for which the near-surface band bending and, accordingly, the near-surface electric field are small [204], STG is mainly due to the excitation of the fast Dember photocurrent in the near-surface region [5,200,201,207].

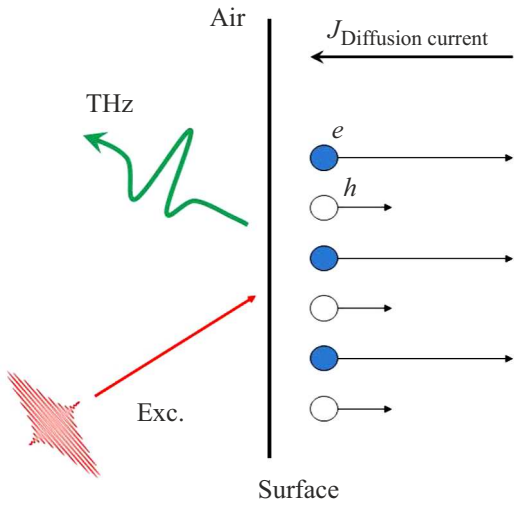

Figure 20. Scheme for THz emission formation due to Dember photocurrent excitation in near-surface region, caused by difference in diffusion coefficients of non-equilibrium electrons and holes. Note that direction of Dember photocurrent will be same in case of semiconductor of both *n*- and *p*-type. THz generation in this case is due to the ultrafast formation and relaxation of the diffusion photocurrent.

When the surface (100) of these crystals is excited by femtosecond laser radiation with wavelength of 800 nm (quantum energy 1.55 eV), THz generation signal for InAs is approximately by 7 times higher than the generation signal from InSb [5]. Such a strong difference in the amplitude of THz emission signals caused by STG in these materials is possibly due to the fact that in InSb some of the photoexcited electrons, during the process of their energy

relaxation, fall into the L-valley, where the effective mass of the electrons significantly greater than in Γ-valley, and thus the total diffusion current of electrons decreases [5]. This explanation is supported by the fact that in InSb crystals the efficiency of STG (in terms of signal amplitude) increases by approximately 6 times when the photoexcitation wave length changes from 800 nm to 1.9 μm [208].

3.2.4. THz generation in structures with $p-n$-junction

Similar to the fast photocurrent of non-equilibrium charge carriers created by femtosecond interband laser photoexcitation in the near-surface region of the crystal (Section 3.2.3, Figure 19), the photocurrent in structure with $p-n$-junction arising during its photoexcitation by ultrashort laser pulses, shall also cause the generation of THz emission.

THz generation of this type was first demonstrated at room temperature on reverse-biased silicon $p-i-n$ photodiodes of large-area [209] optimized for wavelength about 600 nm. In the experiments [209] Si $p-i-n$-structures were excited by pulses with width of 70 fs with central wavelength of 615 nm, followed with frequency of 100 MHz. The structures were excited by oblique (60°) incidence of unfocused laser radiation with average power about 15 mW. RD-SOS-based PCA was used as the coherent THz detector. The spectrum of the recorded THz emission extended to frequencies about 1.4–1.5 THz (at a level of 0.01).

Papers [210,211] inform about observation and study of THz emission generation at room temperature in $p-n$-heterostructures based on a-Si:H|c-Si and a-Si:H|a-SiC:H|c-Si when excited by femtosecond laser pulses with wavelength of 800 nm. The studied structures were solar cells obtained using heterostructure (HJT) technology, capturing significant part of the solar emission spectrum and having rather high efficiency [212]. The structures were excited at an 45-degree oblique incidence of emission (p-polarization) of Ti-sapphire laser generating pulses with width about 15 fs with repetition rate of 80 MHz. Pump radiation with pulse energy of 2–5 nJ was focused onto the upper layer of the structure into a spot with size about 100–250 μm. THz emission was recorded in the direction of mirror reflection of the pump laser beam. THz emission was detected by electro-optical sampling of THz waveforms in ZnTe crystal 1 mm thick. THz emission was observed upon the reverse bias of structures, and its intensity increased significantly with increase in bias voltage. The amplitude spectrum of the observed emission extends to frequencies about 2.2 THz (at a level of 0.01). A non-monotonic dependence of the THz emission pulse amplitude on the laser excitation intensity was observed (dependence with a maximum followed by a signal decreasing [211]), which is fully explained by the effect of electric field screening in $p-n$-heterostructure with non-equilibrium carriers at high level of photoexcitation. At optimal intensity of interband laser photoexcitation, the pulses amplitude of THz emission observed in the studied $p-n$-heterostructures is comparable to THz emission generated in n-InAs crystals, widely used as emitters in THz-TDS systems (Section 3.2.3). In addition to the possible practical application of the detected THz emission in $p-n$-heterostructures based on a-Si:H|c-Si and a-Si:H|a-SiC:H|c-Si, the studies of THz generation processes can be used to study the behavior details of non-equilibrium charge carriers at subpicosecond times in complex structures of HJT solar cells [210,211].

The paper [213] reported the observation of THz emission generation under femtosecond laser excitation with central wavelength of 1.56 μm of InGaAs photodiode structures grown by MOCVD on InP substrates. LT-GaAs-based PCA, gated by pulses of the second harmonic of the pump laser (780 nm), was used as emission detector. The structures were excited through InP substrate with oblique (45°) incidence on it of exciting laser radiation. THz emission was recorded in the passage direction of the structure, collinear with the direction of the exciting laser beam. In this case, hemispherical silicon lens was fixed on the output surface of the structure. The amplitude spectrum of the generated THz emission extended to frequency about 3 THz. At reverse bias voltage of 3 V and average pump radiation power of 9 mW, at frequency of about 1 THz, the amplitude of THz emission field generated in the studied structures of InGaAs photodiodes is almost by order of magnitude higher than the THz emission signal from the surface of n-InAs crystals under similar photoexcitation conditions. The paper [213] also noted non-monotonic dependence of the pulse amplitude of THz emission on the photoexcitation intensity caused by the influence of the screening effect of the electric field in the structure by non-equilibrium charge carriers.

The interesting version of THz emitter based on GaAs|AlGaAs $p-i-n-i$-heterostructure, designed to operate without applying the bias voltage and at $T = 300$ K, was demonstrated in the paper [214]. The structure was grown by MBE on n^+-GaAs substrate and contained 5 periods of undoped layers $Al_xGa_{1-x}As|Al_{0.45}Ga_{0.55}As$ (100 nm). Between the layers $Al_xGa_{1-x}As$ and $Al_{0.45}Ga_{0.55}As$ by alternating method the layers p^+-GaAs and n^+-GaAs were grown (doping level about $2 \cdot 10^{18}$ cm^{-3}) (δ-doped layers). The thicknesses of δ-doped layers were 10 nm, with the exception of the first (from the air-structure interface layer) p^+-GaAs 40 nm thick. Thickness of the first layer $Al_xGa_{1-x}As$ was 250 nm, and of next layers 280 nm each. Parameter x in layers $Al_xGa_{1-x}As$ varied from 0.08 (first layer) to 0 (last layer). Such design $p-i-n-i$ GaAs|AlGaAs of THz emitter was suggested in [215]. According to the idea and simulation results of the paper [215], during femtosecond laser photoexcitation of structure by laser radiation with wavelength about 800 nm, non-equilibrium electrons and holes are generated only in i-layers (in $Al_xGa_{1-x}As$ layers), in which due to δ-doping a strong electric field with strength about 50 kV/cm is created. In $Al_{0.45}Ga_{0.55}As$ layers, with the opposite direction of the electric field, there is no generation of non-equilibrium carriers, similar to the situation in the shaded areas of PCA

with interdigital electrodes (Section 3.2.1). As a result, THz emission generated during the acceleration of non-equilibrium carriers in $Al_xGa_{1-x}As$ layers is summed up coherently. In this case, the movement of non-equilibrium carriers along the normal to the heteroboundaries is limited due to the presence of potential barriers. As a result, according to [215], conditions are created in the structure for the excitation of coherent plasma oscillations in a system non-equilibrium electrons and holes, which leads to a significant increase in the intensity of the generated THz emission. Simulations carried out in [215] showed that for such a THz emitter based on $p-i-n-i$ GaAs|AlGaAs heterostructure, one can expect increase in THz generation efficiency by two orders of magnitude compared to THz generation efficiency from the surface of semiconductors. In the experiments of the paper [214] the studied $p-i-n-i$-heterostructures were excited at obliqie (45°) incidence of femtosecond laser radiation with wavelength of 780 nm (Ti-sapphire laser generating pulses with width of < 100 fs and repetition rate of 82 MHz was used). The generated THz emission was recorded in the direction of mirror reflection of the pump laser beam and measured using optical-acoustic receiver (Golay cell). The maximum average power of the generated THz emission was about $1.25\,\mu$W with average pump emission power of 400 mW [214]. As the photoexcitation intensity increases, the generated THz emission intensity first increases, then passes through a maximum (according to the data of the paper [214], the maximum corresponds to the photoexcitation energy density about $0.7\,\mu J/cm^2$), followed by a strong decrease in THz emission intensity. The non-monotonic dependence of THz emission intensity on the pump intensity is also explained by the influence of the screening effect of the electric field in the structure by non-equilibrium charge carriers. Paper [214] compared the efficiency of THz generation in $p-i-n-i$-heterostructure GaAs|AlGaAs with THz efficiency generation in n-InAs (100) and p-InAs (111) (in latter case THz generation was caused by both OR effect, and by Dember effect contribution). According to data of paper [214], at photoexcitation energy density below $0.7\,\mu J/cm^2$ THz generation efficiency in $p-i-n-i$-heterostructure GaAs|AlGaAs exceeds by about 5 times and by 1.5 times STG efficiency in n-InAs (100) and in p-InAs (111), respectively.

3.2.5. Generation in structures with quantum wells and superlattices

During interband photoexcitation of low-dimensional semiconductor structures with ultrashort laser pulses, the coherent THz emission is also generated. Study of the processes of such THz generation now constitutes a separate, large scientific direction. During studies of THz emission generation under femtosecond photoexcitation of structures with quantum wells and superlattices at low temperatures bright effects of a purely quantum nature were observed, including the phenomenon of quantum beats during coherent excitation of several energy levels in the system, Bloch oscillations of electrons in SLs, coherent nutations of the population of exciton states in strongly coupled exciton-photon systems (see, for example, [5] and other references there). A number of such results, which may also have practical significance, will be discussed below.

In the paper [216] THz generation was excited by radiation from femtosecond Ti-sapphire laser (wavelength 805 nm, pulse width about 160 fs) in double asymmetric tunnel-connected (DATC) QWs GaAs|AlGaAs at a temperature of 10 K. THz experiments were carried out with oblique (45°) incidence of laser radiation on the structure. THz emission caused by the excitation of charge oscillations in the DATC-QW was detected. The structure under study was obtained by MBE on n^+-GaAs substrate and contained 10 DATC QW GaAs 14 nm and 10 nm wide, separated by $Al_{0.2}Ga_{0.8}As$ barrier 2.5 nm wide. In this case, the quantum wells were in the electric field, the strength of which was selected to equalize the position of the size quantization levels of electrons ($n = 1$) in the wide and narrow wells. To create the electric field in the structure a Schottky barrier was created on it (a translucent chromium layer 5 nm thick was deposited on the structure surface [216]). The structure design was chosen such that the electron energy levels in the wide and narrow wells are equalized under reverse bias at the Schottky barrier. As a result of tunnel connection of electron states in wide and narrow quantum wells, energy levels ($n = 1$) are split by value ΔE. Femtosecond laser radiation with spectral width greater than ΔE but less than the energy difference of interband transitions in narrow and wide wells causes the excitation of coherent charge oscillations between quantum wells: an electron packet created by pumping in wide well, will tunnel into the narrow well and back with frequency equal to $\Delta E/h$ [216], where h — Planck's constant. Time-dependent polarization P associated with coherent charge oscillations leads to the emission of electromagnetic THz wave, the amplitude of the electric field in the wave zone is proportional to $\partial^2 P/\partial t^2$. The THz-TDS technique used in [216] made it possible to observe up to 14 cycles of coherent charge oscillations in the studied QWs.

In a single QW GaAs|$Al_{0.3}Ga_{0.7}$ As THz generation was demonstrated, which was caused by the appearance of charge oscillations in the system upon coherent excitation of excitons with both light (lh) and heavy (hh) hole (quantum beats between lh- and hh-excitons) [217]. The structure under study was a Schottky diode metal $-i-n^+$, in i-region of which there were 15 periods of GaAs quantum wells 17.5 nm wide, separated by $Al_{0.3}Ga_{0.7}As$ barriers 15 nm wide. The Schottky barrier was created by applying semitransparent chromium layer 5 nm thick to the GaAs layer (20 nm) covering the structure. A constant electric field in the region, where QWs were located, was created by applying voltage between the metal layer and n^+-GaAs substrate. The electric field strength in QW region was

determined from the photocurrent spectra in the structure [217] and ranged from 4 to 32 kV/cm. The structure under study was excited by radiation from femtosecond Ti|sapphire laser, tunable in wavelengths near 800 nm. The laser pulses width was about 80 fs, the repetition rate was 82 MHz, and the maximum emission energy in the pulse was about 15 nJ. Experiments on THz generation were carried out at $T = 10$ K with oblique 45°-incidence of femtosecond laser radiation on the structure under study. It was established in experiments [217] that when the energy band of pump laser generation (spectral width about 26 meV) is overlapped with *lh*- and *hh*-exciton transitions (calculated value of *lh*−*hh*-splitting in zero field is about 6 meV and increases with field increasing [217]), long-term oscillations are clearly visible in the waveforms of the generated THz emission, they decay over time about several picoseconds. It was also established that such oscillations disappear when the laser generation energy band is not overlapped with the region of *lh*- and *hh*-exciton transitions. The oscillating part of THz waveforms gives spectrum of THz emission with central frequency tunable from 1.4 to 2.6 THz when the bias field strength changes. Besides, the dependence of the central frequency of such THz generation on the field strength in QW is in good agreement with the calculated splitting of the energies of *lh*- and *hh*-excitons. Thus, it was shown that coherent photoexcitation of two types of excitons in QW leads to the excitation of charge oscillations and, accordingly, to a time-varying dipole moment, which, in turn, emits THz electromagnetic wave.

THz emission generation caused by the excitation of quantum beats in structures with single modulated-doped parabolic quantum well (PQW) was observed in the paper [218]. InGaAs|AlGaAs PQW 13.8 nm wide was grown by MBE method on GaAs substrate. The material in the center of PCW had the composition $In_{0.125}Ga_{0.875}As$, and at the edges of the well—- $Al_{0.3}Ga_{0.7}As$. The calculated value of the energy gap between equidistant levels of size quantization of electrons in such PQW is about 10 meV [218]. QW was in the electric field of the Schottky barrier, which was created by depositing a semitransparent layer of NiCr 7 nm thick on the surface of the structure (note that the presence of a strong electric field is important for the excitation of quantum beats, for example, due to the fact that without field in symmetric structure with three-level system the quantum beats are prohibited [218]). THz emission was excited by oblique (60°) incidence of femtosecond laser radiation on the structure. The Ti-sapphire laser was used, tunable in wavelengths near 800 nm, generating pulses with width about 10 fs with repetition rate of 75 MHz. The experiments on THz generation were carried out at temperature of 6 K. The characteristic electric field strength in the PQW was about several kV/cm. Numerous fast oscillations were observed in the waveforms of the generated THz emission, which continued for about 6 ps. In the spectrum of the generated THz emission a sharp peak was observed at frequency of 2.82 THz, which according to its spectral position coincided

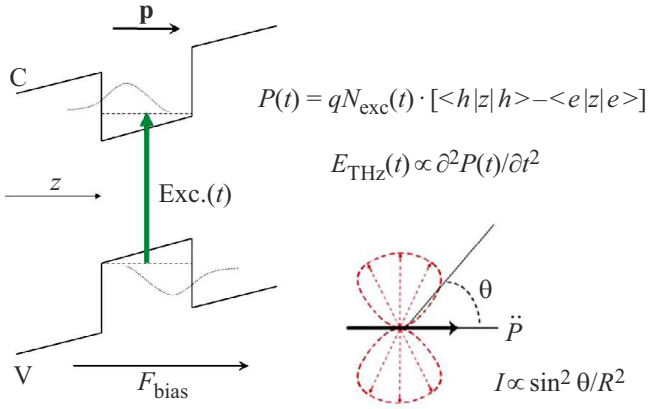

Figure 21. Scheme of THz generation during photoexcitation by ultrashort laser pulses of QW placed in strong electric field. The envelopes of the wave functions of electrons and holes in such a QW are also shown schematically. The electric field shifts the centers of the electron and hole wave functions to opposite sides of QW, creating dipole moment $P(t)$.

with the peak of intersubband electronic transitions in the absorption spectrum of the studied PQWs. The amplitude of the detected THz oscillations increased with increase in electric field strength in the PQW, but the frequency of these oscillations remained constant. The combination of experimental data and the results of numerical calculations allowed the authors of Ref. [218] to conclude that the observed THz emission is caused by intersubband charge oscillations of non-equilibrium electrons in the PQW, excited by ultrashort pulses of interband pumping [218].

In the electric field optical generation of electrons and holes is possible in polarized states, in which the electron and hole are separated in coordinate space, which leads to the appearance of fast dipole moment and, accordingly, to THz generation [185]. It is quite difficult to realize such situation in the bulk of semiconductor, but in quantum wells located in the external electric field, this is quite feasible (Figure 21). The paper [219] for the first time demonstrated THz generation caused by creation of polarized electron-hole pairs in single, undoped GaAs|AlGaAs quantum wells placed in the electric field. The experiments were carried out at $T = 77$ K on structures containing 82 periods of GaAs quantum wells 14.5 nm wide, separated by barriers $Al_{0.3}Ga_{0.7}As$ 10.2 nm wide, grown by MBE method on silicon substrates. The electric field in the structure, as in the above-mentioned papers, was created by applying bias voltage to the Schottky barrier, which was formed by depositing the semitransparent chromium layer on surface of the structure. For photoexcitation the Ti-sapphire laser was used, tunable in wavelengths near 800 nm, generating pulses with width about 100 fs with pulse energy about 1.5 nJ [219]. The experiments were carried out with oblique (45°) incidence of laser radiation with average power about 50 mW on the surface of the structure under study (spot size ~ 1 mm). THz emission was recorded by

PCA-based receiver. The electric field strength in QW was determined from the spectra of the stationary photocurrent in the structures and ranged from -10 to $+25$ kV/cm [219]. In the range of photoexcitation energy densities used in the experiments [219] ($< 0.15\,\mu$J/cm^2), the amplitude of THz signal increased linearly with intensity increasing of the exciting laser radiation. The spectrum of the generated THz emission occupies the band from 0.1 to 3.2 THz with a maximum at frequency about 1.5 THz and, which is very important, does not change with changes in the electric field strength. THz waveforms contain almost one cycle of electromagnetic oscillations and change polarity when the direction of the electric field changes. The amplitude of THz signal increases with field strength increasing, but reaches saturation at field strength greater than 15 kV/cm. Experimental data [219] allow the authors to conclude that the observed THz emission is due to the generation of polarized electron-hole pairs in QW located in external field. The amplitude of THz signal generated from QWs under study in field of 15 kV/cm was only by 2 times weaker than STG signal from semi-insulating GaAs, measured under identical conditions.

Papers [220,221] studied THz emission generation in structures with GaAs|$Al_{0.37}Ga_{0.83}As$ quantum wells located in electric field with strength of up to about 42 kV/cm. The experiments were carried out at temperature of 300 K. Structures containing 45 periods of undoped QWs 29 nm wide, separated by barriers also 29 nm wide, grown by the MBE method on n^+-GaAs substrate, were studied. As in other mentioned above papers on the study of THz generation in QWs, the electric field in the structure under study was created by applying the bias voltage to the Schottky barrier, which was formed by depositing semitransparent layer of chromium 10 nm thick on the GaAs (10 nm) layer covering the structure. The structures were excited at oblique (45°) incidence of emission of Ti-sapphire laser generating pulses with width about 12 fs with central wavelength of 792 nm, and followed with repetition rate of 80 MHz. Maximum density of photoexcitation energy in pulse was about $23\,\mu$J/cm^2. THz emission was detected in the direction of mirror reflection of the pump laser beam and measured by electro-optical sampling of waveforms in ZnTe (110) crystal 1 mm thick. The properties of the observed THz emission indicate that THz generation is also caused by the creation using optical pumping of the polarized electron-hole pairs in quantum wells located in electric field. At bias voltage on the structure of 10 V, which corresponds to electric field strength in QW region about 42 kV/cm, the amplitude of the observed THz signal is by 4 times greater than the THz signal generated in the test sample of „parent“ n^+-GaAs substrate, but it is weaker by approximately 5 times then THz signal from „reference“ THz emitter based on n-InAs [162,203]. It was found that at photoexcitation energy densities above $2\,\mu$J/cm^2 the dependence of THz signal amplitude on the pump intensity becomes sublinear. The observed sublinearity is due to the occurrence of the electric field screening effect in quantum wells, i. e. partial compensation of the external field in QW by the field of polarized electrons and holes. A theoretical model of dynamic screening of the electric field in GaAs|AlGaAs quantum well by non-equilibrium electron-hole pairs was developed, which, taking into account actual experimental conditions, quite satisfactorily describes the observed dependence of THz emission amplitude on the pump intensity. Add also that in the developed model there are no fitting parameters [221]. When comparing theory with experiment, only one parameter was used, i. e. the scale factor. The introduction of scale factor when comparing calculation with experiment is required in any case, for example, to relate the amplitudes of THz field in the near and far zones.

In experiments [222] with femtosecond photoexcitation of structures with GaAs|AlGaAs SL, coherent THz emission caused by Bloch's oscillations (BO) of electrons in SL with electrical bias was discovered for the first time.

Especially note here that the phenomenon of oscillatory motion of free electrons in crystals in the presence of strong constant electric field (BO), predicted in papers [223,224], was long considered as a promising basis for creating sources of THz emission with electrical excitation. The BO phenomenon is a direct consequence of the band theory of solids and Bloch's theorem. Bloch's oscillations are caused by electrons acceleration by the electric field and their Bragg reflection at the boundary of the Brillouin zone of the crystal. The oscillation frequency ν is determined by the field strength F and the crystal lattice period d, so that

$$h\nu = eFd, \tag{6}$$

where e — electron charge, h — Planck's constant. The threshold field F_t of BO mode corresponds to the condition $elF_t = \Delta E$, where l — electron mean free path, ΔE — width of the allowed electronic band (conduction band in bulk crystal or mini-band in structure with SL). Quantum consideration of the problem shows [225], that in strong field electrons turn out to be localized, and the electron energy spectrum is a Wannier-Stark ladder of equidistant discrete levels with splitting energy corresponding to the equation (6). Thus, Wannier-Stark localization (WSL) is the frequency (or energy) equivalent of Bloch's oscillations. In bulk crystals, BO requires giant electric fields and is therefore unobtainable. L. Esaki and R. Tsu [11] drew attention to the fact that in SL, due to the relatively small width of the electron miniband ΔE and long period d the BO phenomenon can be realized in easily achievable electric fields. WSL occurrence in GaAs|AlGaAs SLs was recorded in a number of papers on electrical transport, as well as on optical spectroscopy (see, for example, [226,227]). Nevertheless, despite numerous attempts (see review [226]), THz emission due to BO of free carriers in SL was not observed until the appearance of the paper [222] in which the use of the THz-TDS technique made it possible to register THz emission caused by the BO.

The experiments [222] were carried out on structures containing 35 periods of GaAs QW 9.7 nm wide, separated

by barriers $Al_{0.3}Ga_{0.7}As$ 1.7 nm thick, grown by MBE method on n^+-GaAs substrate. The electric field in the SL was created by applying a reverse bias voltage to the Schottky contact. The Schottky barrier was formed by depositing the semitransparent chromium layer (5 nm) to the surface of the structure. The calculated width of the first mini-band for the SL used is 19 meV for electrons and 2 meV for heavy holes [222]. The fact that WSL mode is achieved in strong electric field in the created SL was monitored by measurements of the photocurrent spectra in the structures at $T = 4$ K. THz emission generation was studied during photoexcitation of structures with radiation from Ti-sapphire laser, generating pulses with width about 100 fs, wavelength of 802 nm, followed with frequency of 76 MHz. THz experiments were carried out at $T = 15$ K with oblique (45°) incidence of femtosecond laser radiation on the structure under study. The level of photoexcitation, according to the data of the paper [222], was such that the density of non-equilibrium electron-hole pairs in QW was significantly lower than $1 \cdot 10^9$ cm^{-2}. At reverse bias voltage on the structure above 1.5 V, numerous oscillations were observed in THz waveforms, the number of them increased with bias voltage increasing. The amplitude of THz signal also increased. In the amplitude spectra of the THz emission an emission line was observed, the frequency of which was varied from 0.5 to 2 THz with bias voltage increasing. Moreover, in the bias voltage range of -2.5 to -3.5 V the THz generation frequency shift was almost linear versus the bias voltage. In parallel with THz measurements (at $T = 15$ K), spectra of electroreflectance were measured on the structures under study, which made it possible to observe the correlation of changes in the Wannier-Stark ladder with changes in the THz emission spectra. The measurements and their analysis allowed the authors of [222] to conclude that the observed THz emission is due to the BO of electrons in SL. Note that in the paper [228], where THz emission in GaAs|AlGaAs SL with wide mini-bands (about 50 and 100 meV) was studied, data were also obtained on THz emission generation associated with BO in SL upon photoexcitation by ultrashort laser pulses.

The impressive results of the papers [222,228] stimulated further studies of THz emission due to BO effect. In the papers of [229,230] the spontaneous THz electroluminescence (EL) caused by BO of electrons in the natural SL (NSL) of silicon carbide under quasi-stationary excitation was detected and studied for the first time. Study of THz emission in structures with NSL of silicon carbide under purely electrical excitation was initiated by V.I. Sankin, who for a long time intentionally studied the WSL phenomenon in the conduction band of silicon carbide polytypes and observed its numerous manifestations in electronic transport (see review [231]). NSL in SiC is a long-scale periodicity of chains of atoms with a cubic or hexagonal environment along the C axis in the form of so-called Ramsdell zigzags [232], which is present in all polytypes of silicon carbide, with the exception of purely cubic (3C-SiC) and purely hexagonal (2H-SiC) polytypes. The NSL periods in such polytypes as 4H-, 6H-, 8H-SiC are equal to 5, 7.5 and 10 Å respectively [231]. A significant difference between the NSL of silicon carbide and classical SLs, such as, for example, GaAs|AlGaAs, is that in the natural lattice there is no scattering of electrons at heterointerfaces.

Experiments [229,230] were conducted on $n^+-n^--n^+$-6H-SiC diode structures. The base n^--layer was grown by sublimation on 6H-SiC (0001) Lely substrate and had a concentration of 10^{15} cm$^{-3} < N_d - N_a < 10^{16}$ cm^{-3} and thickness about 2 μm. The concentration $N_d - N_a$ in the substrate (n^+-region) was about $2 \cdot 10^{18}$ cm^{-3}, and its thickness was 200 μm. The upper n^+-contact layer with concentrations $N_d - N_a \sim 10^{20}$ cm^{-3} was created on n^--layer by implanting nitrogen ions with subsequent annealing and was 150 nm thick. Using photolithography and dry etching methods, mesa structures with an area about $3 \cdot 10^{-5}$ cm^2 were prepared on the substrate. The upper electrical contact to the mesastructure was continuous, and the second contact, common, was located on the free part of the substrate surface (Figure 22, *a*). The insulating layer on the substrate and on the periphery of the mesastructures was formed due to irradiation with protons. The samples under study were mounted on the cold finger of the helium optical cryostat ($T \approx 7$ K), optimized for THz region of the spectrum. THz emission was recorded through the substrate in the direction of normal to its surface within the spatial angle $\sim 30°$. A negative bias was applied to the samples (negative potential on the upper n^+-layer, see Figure 22, *a*) in the form of bursts of rectangular pulses with repetition rate of 75 Hz and the individual burst duration 6.7 ms. This bias was used to minimize the influence of lattice heating on the measurement results. THz emission was measured with a liquid helium-cooled silicon bolometer using the synchronous detection method. THz-EL spectra were recorded using Fourier spectrometer. Intense THz electroluminescence was observed when the bias voltage amplitude on the mesastructure exceeded ~ 190 V. The presence of such a threshold is associated with the breakdown of impurity centers in the upper n^+-layer of the structure, which ensures the subsequent injection of free carriers (electrons) into SiC NSL [229]. After impurity breakdown is achieved, the voltage in the structure is redistributed, and part of it is applied to the base region of the structure (n^--layer). In this case, THz emission appears, its intensity increases linearly with current increasing through the structure [230]. Estimates of the spectrum-integrated pulsed power of THz emission give a value about 10 μW at 46.2 W (0.21 A, 220 V) of supplied pulsed electrical power, and the corresponding external quantum output of THz-emission is ~ 0.01 photons/electron ($\sim 1\%$) [229,230]. The characteristic spectra of the detected THz EL for 6H-SiC structures with NSL at several values of the bias voltage are shown in Figure 22, *b*.

The spectrum of the detected THz emission contains a single line, its maximum shifts to the high-frequency region with increase in bias voltage according to a law close to linear, with the rate about 32 μeV/V [229,230]. In this case,

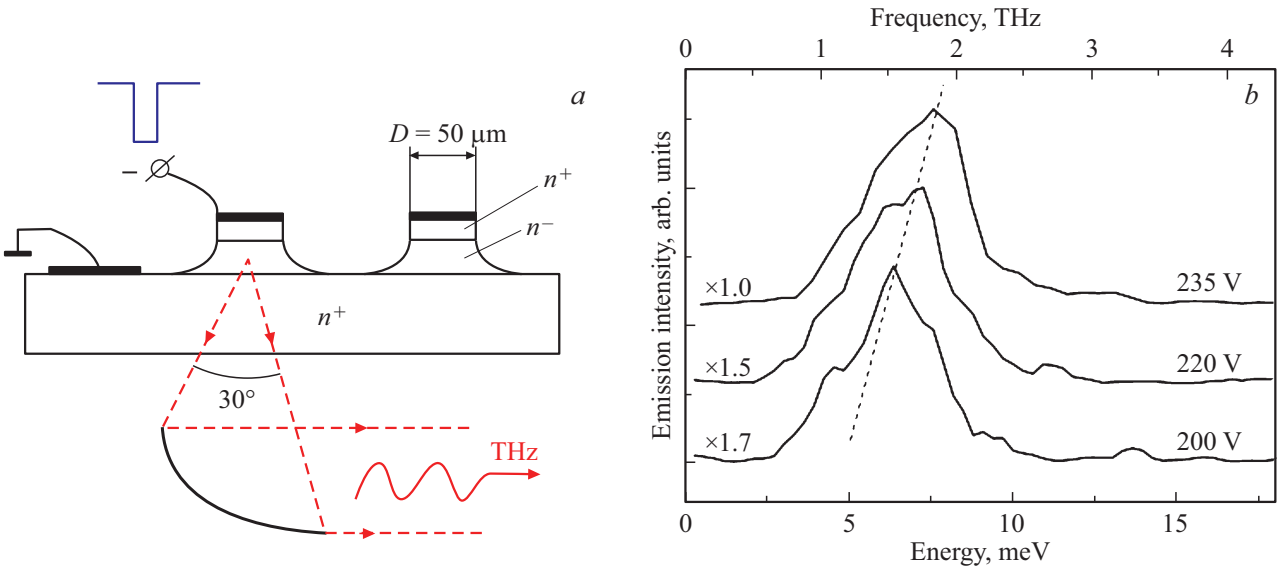

Figure 22. *a* — schematic representation of the studied $n^+-n^--n^+$ 6H-SiC mesa structures with NSL and geometry THz-EL of experiment. *b* — THz-EL spectra of $n^+-n^--n^+$ 6H-SiC structures with NSL at several bias voltages. $T \approx 7$ K. The spectra are normalized to the maximum and shifted vertically for clarity. Dotted line — „guide“ for the eyes.

the THz emission linewidth remains practically constant and equal to ~ 2.9 meV (0.7 THz) when the bias voltage changes from 200 to 240 V [229,230]. It is also important to note that the shape of THz emission line is much better described by Lorentz profile than by Gauss profile [230]. Using specially prepared 6H-SiC structures that make it possible to observe THz emission from the end of the structures, it was found that THz EL is linearly polarized along the electric field direction (and *C* axis) with a degree of polarization about 50%. The combination of properties of the detected THz emission makes it possible to associate it with the excitation of stationary BO electrons in SiC NSL. In the paper [230] the internal quantum yield of spontaneous THz emission due to optical transitions between levels of the Wannier-Stark ladder in NSL of 6H-SiC polytype was theoretically calculated. The calculation gave a value about 4%, which is in very good agreement with the experimental data on THz-EL, taking into account the non-optimal conditions for obtaining THz-EL from the studied 6H-SiC structures. The injection of electrons from the n^+-contact layer into the base layer of the studied structures with NSL apparently facilitates the formation of a uniform electric field distribution in the NSL region even under WSL regime [233], thus creating conditions for observing THz emission caused by BO. Paper [234] observed THz electroluminescence caused by BO of electrons on structures with NSL SiC of other polytypes — 8H and 4H.

4. Conclusion

Over the past three decades of studies in the field of THz emission phenomena in semiconductors, a number of effective methods for generating THz emission have been found, many of which were discussed above.

This review does not include such rapidly developing area of THz studies and practical development as photomixing (PM). PM technology is based on the THz emission generation in semiconductor photoresistor based on the material with short lifetime of non-equilibrium charge carriers (in the subpicosecond time range) due to the beats excitation in the photocurrent at THz frequencies during photoexcitation by the radiation of two continuous lasers with different wavelengths. The photoresistor is integrated with antenna, which provides emission of electromagnetic THz waves into the ambinient space. By tuning the wavelengths of pump lasers in PM-based THz sources, it is possible to cover the frequency range from 0.1 to 3 THz [5]. PM-based sources can be applied for THz spectroscopy of various objects, although the spectral resolution in THz spectrometers based on PM is inferior to the resolution achieved, for example, in THz spectrometers using emitters based on microwave frequency multiplication (Section 3.1.1). At the same time, the efficiency of converting optical power into THz emission power for PM-based THz emitters is quite low and, at best, is about 10^{-6}–10^{-5} [5]. There are a number of good reviews on PM technology, including [5,235], as well as a relatively new review [236].

Some of the methods discussed in this review for THz emission generation in semiconductors are already used to solve problems of THz diagnostics and spectroscopy, and the other part may find application in the future. Over these years, a whole field of science has been formed — THz optoelectronics, one of the most important sections of which relates to the technology of THz emission generation in semiconductors and semiconductor structures. Thanks to

the successes of THz optoelectronics, the „THz gap“ in the electromagnetic spectrum, which was much talked about in the 90s and early 2000s in the context of the difficulties of obtaining radiation in this spectral range, has now become largely achievable.

Conflict of interest

The author declares that he has no conflict of interest.

References

[1] B. Ferguson, X.-C. Zhang. Nature Mater. **1**, *1*, 26 (2002).
[2] P.H. Siegel. IEEE Trans. Microwave Theor. Technques **50**, *3*, 910 (2002).
[3] M. Hangyo. Jpn J. Appl. Phys. **54**, *12*, 120101 (2015).
[4] Terahertz Spectroscopy and Imaging / Eds K.-E. Peiponen, J.A. Zeitler, M. Kuwata-Gonokami. Springer-Verlag, Berlin, Heidelberg (2013). 641 p.
[5] Terahertz Optoelectronics / Ed. K. Sakai. Springer-Verlag, Berlin (2005). 387 p.
[6] F. Sizov. Semicond. Sci. Technol. **33**, *12*, 123001 (2018).
[7] S.R. Kasjoo, M.B. Mohd Mokhar, N.F. Zakaria, N.J. Juhari. AIP Conf. Proceed. **2203**, *1*, 020020 (2020).
[8] J. Faist, F. Capasso, D.L. Sivco, C. Sirtori, A.L. Hutchinson, A.Y. Cho. Sci. **264**, *5158*, 553 (1994).
[9] R. Kohler, A. Tredicucci, F. Beltram, H.E. Beere, E.H. Linfield, A.G. Davies, D.A. Ritchie, R.C. Iotti, F. Rossi. Nature **417**, *6885*, 156 (2002).
[10] R.F. Kazarinov, R.A. Suris. Sov. Phys. Semicond. **5**, *1*, 707 (1971).
[11] L. Esaki, R. Tsu. IBM J. Res. Dev. **14**, *1*, 61 (1970).
[12] F. Capasso, C. Gmachl, R. Paiella, A. Tredicucci, A.L. Hutchinson, D.L. Sivco, J.N. Baillargeron, A.Y. Cho, H.C. Liu. IEEE J. Select. Top. Quant. Electron. **6**, *6*, 931 (2000).
[13] A.Y. Cho. Molecular beam epitaxy. AIP, N.Y. (1994). 310 p.
[14] F. Capasso, A.Y. Cho. Surf. Sci. **299**–**300**, 878 (1994).
[15] F. Capasso, K. Mohammed, A.Y. Cho. Appl. Phys. Lett. **48**, *7*, 478 (1986).
[16] F. Capasso, J. Faist, C. Sirtori. J. Math. Phys. **37**, *10*, 4775 (1996).
[17] B.S. Williams. Nature Photonics **1**, *9*, 517 (2007).
[18] M.A. Belkin, F. Capasso. Physica Scripta **90**, *11*, 118002 (2015).
[19] B. Wen, D. Ban. Progress. Quant. Electron. **80**, 100363 (2021).
[20] L. Sirigu, A. Rudra, E. Kapon, M.I. Amanti, G. Scalari, J. Faist. Appl. Phys. Lett. **92**, *18*, 181111 (2008).
[21] M.I. Amanti, G. Scalari, R. Terazzi, M. Fischer, M. Beck, J. Faist, A. Rudra, P. Gallo, E. Kapon. New J. Phys. **11**, *12*, 125022 (2009).
[22] K. Fujita, M. Yamanishi, S. Furuta, K. Tanaka, T. Edamura, T. Kubis, G. Klimeck. Opt. Express **20**, *18*, 20647 (2012).
[23] T.A. Bagaev, M.A. Ladugin, A.A. Marmalyuk, A.I. Danilov, D.V. Ushakov, A.A. Afonenko, A.A. Zaytsev, K.V. Maremyanin, S.V. Morozov, V.I. Gavrilenko, R.R. Galiev, A.Yu. Pavlov, S.S. Pushkarev, D.S. Ponomarev, R.A. Khabibullin. Tech. Phys. Lett. **122**, *5*, 45 (2022).
[24] C.A. Curwen, J.L. Reno, B.S. Williams. Nature Photon. **13**, *12*, 855 (2019).
[25] Y. Jin, J.L. Reno, S. Kumar. Optica **7**, *6*, 708 (2020).
[26] C. Sirtori, S. Barbieri, R. Colombelli. Nature Photon. **7**, *9*, 691 (2013).
[27] A. Khalatpour, A.K. Paulsen, C. Deimert, Z.R. Wasilewski, Q. Hu. Nature Photon. **15**, *1*, 16 (2021).
[28] A. Khalatpour, Man Chun Tam, S.J. Addamane, J. Reno, Z. Wasilewski, Q. Hu. Appl. Phys. Lett. **122**, *16*, 161101 (2023).
[29] G. Scalari, L. Ajili, J. Faist, H. Beere, E. Linfield, D. Ritchie, G. Davies. Appl. Phys. Lett. **82**, *19*, 3165 (2003).
[30] B.S. Williams, H. Callebaut, S. Kumar, Q. Hu, J.L. Reno. Appl. Phys. Lett. **82**, *7*, 1015 (2003).
[31] E. Dupont, S. Fathololoumi, Z. Wasilewski, G. Aers, S. Laframboise, M. Lindskog, S. Razavipour, A. Wacker, D. Ban, H.C. Liu. J. Appl. Phys. **111**, *7*, 073111 (2012).
[32] D.V. Ushakov, A.A. Afonenko, A.A. Dubinov, V.I. Gavrilenko, I.S. Vasil'evskii, N.V. Shchavruk, D.S. Ponomarev, R.A. Khabibullin. Quant. Electron. **48**, *11*, 1005 (2018).
[33] B.S. Williams, S. Kumar, H. Callebaut, Q. Hu, J.L. Reno. Appl. Phys. Lett. **83**, *11*, 2124 (2003).
[34] R.A. Khabibullin, N.V. Shchavruk, A.Yu. Pavlov, D.S. Ponomarev, K.N. Tomosh, R.R. Galiev, P.P. Maltsev, A.E. Zhukov, G.E. Cirlin, F.I. Zubov, Zh.I. Alferov. Semiconductors **50**, *10*, 1377 (2016).
[35] T. Grange, D. Stark, G. Scalari, J. Faist, L. Persichetti, L. Di Gaspare, M. De Seta, M. Ortolani, D.J. Paul, G. Capellini, S. Birner, M. Virgilio. Appl. Phys. Lett. **114**, *11*, 111102 (2019).
[36] M.I. Amanti, G. Scalari, R. Terazzi, M. Fischer, M. Beck, J. Faist, A. Rudra, P. Gallo, E. Kapon. New J. Phys. **11**, *12*, 125022 (2019).
[37] S.A. Lynch, R. Bates, D.J. Paul, D.J. Norris, A.G. Cullis, Z. Ikonic, R.W. Kelsall, P. Harrison, D.D. Arnone, C.R. Pidgeon. Appl. Phys. Lett. **81**, *9*, 1543 (2002).
[38] D. Stark, M. Mirza, L. Persichetti, M. Montanari, S. Markmann, M. Beck, T. Grange, S. Birner, M. Virgilio, C. Ciano, M. Ortolani, C. Corley, G. Capellini, L. Di Gaspare, M. De Seta, D.J. Paul, J. Faist, G. Scalari. App. Phys. Lett. **118**, *10*, 101101 (2021).
[39] C. Deutsch, M. Krall, M. Brandstetter, H. Detz, A.M. Andrews, P. Klang, W. Schrenk, G. Strasser, K. Unterrainer. Appl. Phys. Lett. **101**, *21*, 211117 (2012).
[40] K. Ohtani, M. Beck, G. Scalari, J. Faist. Appl. Phys. Lett. **103**, *4*, 041103 (2013).
[41] M. Fischer, G. Scalari, C. Walther, J. Faist. J. Cryst. Growth **311**, *7*, 1939 (2009).
[42] H. Hirayama, W. Terashima, T.-T. Lin, M. Sasaki. Proc. SPIE **9382**, 938217 (2015).
[43] Z. Loghmari, M. Bahriz, A. Meguekam, R. Teissier, A.N. Baranov. Electron. Lett. **55**, *3*, 144 (2019).
[44] Z. Loghmari, M. Bahriz, A. Meguekam, H. Nguyen Van, R. Teissier, A.N. Baranov. Appl. Phys. Lett. **115**, *15*, 151101 (2019).
[45] M.A. Belkin, F. Copasso, A. Belyanin, D.L. Sivco, A.Y. Cho, D.C. Oakley, C.J. Vineis, G.W. Turner. Nature Photon. **1**, *5*, 288 (2007).
[46] M. Razeghi, Q.Y. Lu, N. Bandyopadhyay, W. Zhou, D. Heydari, Y. Bai, S. Slivken. Opt. Express **23**, *7*, 8462 (2015).
[47] S.H. Koenig, R.D. Brown. Phys. Rev. Lett. **4**, *4*, 170 (1960).
[48] I. Melngailis, G.E. Stillman, J.O. Dimmock, C.M. Wolf. Phys. Rev. Lett. **23**, *19*, 1111 (1969).

[49] T.V. Adam, R.T. Troeger, S.K. Ray, P.-C. Lv, J. Kolodzey. Appl. Phys. Lett. **83**, *9*, 1713 (2003).
[50] P.-C. Lv, R.T. Troeger, S. Kim, S.K. Ray, K.W. Goossen, J. Kolodzey, I.N. Yassievich, M.A. Odnoblyudov, M.S. Kagan. Appl. Phys. Lett. **85**, *17*, 3660 (2004).
[51] A.V. Andrianov, A.O. Zakhar'in, I.N. Yassievich, N.N. Zinov'ev. JETP Lett. **79**, *8*, 365 (2004).
[52] P.C. Lv, X. Zang, J. Kolodzey, A. Powell. Appl. Phys. Lett. **87**, *24*, 241114 (2005).
[53] A.V. Andrianov, A.O. Zakhar'in, I.N. Yassievich, N.N. Zinov'ev. JETP Lett. **83**, *8*, 351 (2006).
[54] G. Xuan, S. Kim, M. Coppinger, N. Sustersic, J. Kolodzey, P.-C. Lv. Appl. Phys, Lett. **91**, **6**, 061109 (2007).
[55] I.V. Altukhov, M.S. Kagan, V.P. Sinis. JETP Lett. **47**, *3*, 164 (1988).
[56] I.V. Altukhov, M.S. Kagan, V.P. Sinis. Opt. Quant. Electr. 23, 2, S211 (1991).
[57] I.V. Altukhov, M.S. Kagan, K.A. Korolev, V.P. Sinis. JETP Lett. **59**, *7*, 476 (1994).
[58] I.V. Altukhov, M.S. Kagan, K.A. Korolev, V.P. Sinis, E.G. Chirkova, M.A. Odnoblyudov, I.N. Yassievich. JETP **88**, *1*, 51 (1999).
[59] M.A. Odnoblyudov, I.N. Yassievich, M.S. Kagan, Yu.M. Galperin, K.A. Chao. Phys. Rev. Lett. **83**, *3*, 644 (1999).
[60] Yu.P. Gousev, I.V. Altukhov, K.A. Korolev, V.P. Sinis, M.S. Kagan, E.E. Haller, M.A. Odnoblyudov, I.N. Yassievich, K-A. Chao. Appl. Phys. Lett. **75**, *6*, 757 (1999).
[61] M.S. Kagan, I.V. Altukhov, V.P. Sinis, S.G. Tomas, K.L. Wang, K.A. Chao, I.N. Yassievich. Thin Solid Films **380**, *1–2*, 237 (2000).
[62] I.V. Altukhov, E.G. Chirkova, V.P. Sinis, M.S. Kagan, Yu.P. Gousev, S.G. Thomas, K.L. Wang, M.A. Odnoblyudov, I.N. Yassievich. Appl. Phys. Lett. **79**, *24*, 3909 (2001).
[63] S.G. Pavlov, R.Kh. Zhukavin, E.E. Orlova, V.N. Shastin, A.V. Kirsanov, H.-W. Hübers, K. Auen, H. Riemann. Phys. Rev. Lett. **84**, *22*, 5220 (2000).
[64] C. Jagannath, Z.W. Grabowski, A.K. Ramdas. Phys. Rev. B **23**, *5*, 2082 (1981).
[65] S.G. Pavlov, H.-W. Hübers, E.E. Orlova, R.Kh. Zhukavin, H. Riemann, H. Nakata, V.N. Shastin. Phys. Status Solidi B **235**, *1*, 126 (2003).
[66] H.-W. Hübers, S.G. Pavlov, H. Riemann, N.V. Abrosimov, R.Kh. Zhukavin, V.N. Shastin. Appl. Phys. Lett. **84**, *18*, 3600 (2004).
[67] J.N. Hovenier, T.O. Klaassen, R.Kh. Zhukavin, D.M. Gaponova, A.V. Muravijov, E.E. Orlova, V.N Shastin, S.G. Pavlov, H.-W. Hübers, H. Riemann, A.F.G. van der Meer. Proceed. Symp. IEEE/LEOS, Benelux Chapter, Amsterdam (2002). P. 167–170.
[68] I.O. Davarishvili, L.M. Dolginov, P.G. Eliseev, I.I. Zasavitsky, A.P. Shotov. Kvantovaya elektron. **4**, 904 (1977) (in Russian).
[69] I.I. Zasavitsky, A.V. Matveenko, B.N. Matsonashvili, V.G. Trofimov. FTP **20**, *1*, 214 (1986) (in Russian).
[70] L.N. Kurbatov, A.D. Britov, S.M. Karavaev, S.D. Sivachenko, S.N. Maksimovskii, I.I. Ovchinnikov, M.M. Rzaev, P.M. Starik. JETP Lett. **37**, *9*, 499 (1983).
[71] K.V. Maremyanin, A.V. Ikonnikov, L.S. Bovkun, V.V. Rumyantsev, E.G. Chizhevskii, I.I. Zasavitskii, V.I. Gavrilenko. Semicond. **52**, *12*, 1590 (2018).
[72] C. Weisbuch, B. Vinter. Quantum Semiconductor Structures. Academ. Press Inc, N.Y. (1991). 252 p.
[73] J. Dimmock, I. Melngailis, A. Strauss. Phys. Rev. Lett. **16**, *26*, 1193 (1966).
[74] C.D. Maxey, I.G. Gate, J.B. Clegg, P.A.C. Whiffin. Semicond. Sci. Technlol. **8**, *1S*, S183 (1993).
[75] M. Zandian, J.M. Arias, R. Zucca, R.V. Gil, S.H. Shin. Appl. Phys. Lett. **59**, *9*, 1022 (1991).
[76] J.M. Arrias, M. Zandian, R. Zucca, J. Singh. Semicond. Sci. Technol. **8**, *1S*, S255 (1993).
[77] B.A. Bernevig, T.L. Huges, S.C. Zhang. Sci. **314**, *5806*, 1757 (2006).
[78] M. Konig, H. Buhmann, L.W. Molenkamp, T.L. Higes, C.-X. Liu, X.L. Qi, S.C. Zhang. Sci. **318**, *5851*, 766 (2007).
[79] S.V. Morozov. Diss. d.f.-m.n. IFM RAN, Nizhny Novgorod (2022). (in Russian)
[80] S.V. Morozov, V.V. Rumyantsev, M.A. Fadeev, M.S. Zholudev, K.E. Kudryavtsev, A.V. Antonov, A.M. Kadykov, A.A. Dubinov, N.N. Mikhailov, S.A. Dvoretsky, V.I. Gavrilenko. Appl. Phys. Lett. **111**, *19*, 192101 (2017).
[81] S.V. Morozov, V.V. Rumyantsev, M.S. Zholudev, A.A. Dubinov, V.Ya. Aleshkin, V.V. Utochkin, M.A. Fadeev, K.E. Kudryavtsev, N.N. Mikhailov, S.A. Dvoretskii, V.I. Gavrilenko, F. Teppe. ACS Photon. **8**, *12*, 3526 (2021).
[82] V.V. Rumyantsev, A.A. Dubinov, V.V. Utochkin, M.A. Fadeev, V.Ya. Aleshkin, A.A. Razova, N.N. Mikhailov, S.A. Dvoretsky, V.I. Gavrilenko, S.V. Morozov. Appl. Phys. Lett. **121**, *18*, 182103 (2022).
[83] G. Alymov, V. Rumyantsev, S. Morozov, V. Gavrilenko, V. Aleshkin, D. Svintsov. ACS Photon. **7**, *1*, 98 (2020).
[84] A.A. Andronov, V.A. Kozlov, L.S. Mazov, V.N. Shastin. JETP Lett. **30**, *9*, 551 (1979).
[85] Yu.L. Ivanov. JETP Lett. **34**, *10*, 515 (1981).
[86] L.E. Vorob'ev, F.I. Osokin, V.I. Stafeev, V.N. Tulupenko. JETP Lett. **35**, *9*, 440 (1982).
[87] Yu.L. Ivanov, Yu.B. Vasiliev. Pis'ma v ZhTF **9**, *10*, 613 (1983). (in Russian)
[88] A.A. Andronov, I.V. Zverev, V.A. Kozlov, Yu.N. Nozdrin, S.A. Pavlov, V.N. Shastin. JETP Lett. **40**, *2*, 804 (1984).
[89] S. Komiyama, N. Iizuka, Y. Akasaka. Appl. Phys. Lett. **47**, *9*, 958 (1985).
[90] A.A. Andronov. FTP **21**, *3*, 1153 (1987). (in Russian).
[91] Opt. Quantum Electron. / Eds E. Gornik, A.A. Andronov. Special Issue **23**, S111 (1991).
[92] J.N. Hovenier, M.C. Diez, T.O. Klaassen, W.T. Wenckebach, A.V. Muravjov, S.G. Pavlov, V.N. Shastin. IEEE Trans. Microwave Theory. Techn. **48**, *4* Part *2*, 670 (2000).
[93] F. Keilmann, V.N. Shastin, R. Till. Appl. Phys. Lett. **58**, *20*, 2205 (1991).
[94] E. Bründermann, H.P. Röser, A.V. Muravjov, S.G. Pavlov, V.N. Shastin. Infrared Phys. Technol. **36**, *1*, 59 (1995).
[95] E. Bründermann, A.M. Linhart, L. Reichertz, H.P. Röser, O.D. Dubon, W.L. Hansen, G. Simain, E.E. Haller. Appl. Phys. Lett. **68**, *22*, 3075 (1996).
[96] A.V. Andrianov, A.O. Zakhar'in, Yu.L. Ivanov, M.S. Kipa. JETP Lett. **91**, *2*, 96 (2010).
[97] A.O. Zakhar'in, A.V. Andrianov, A.Yu. Egorov, N.N. Zinov'ev. Appl. Phys. Lett. **96**, *21*, 211118 (2010).
[98] A.O. Zakhar'in, A.V. Bobylev, A.V. Andrianov. Semicond. **46**, *9*, 1135 (2012).
[99] Y. Oyama, H. Dezaki, Y. Shimizu, K. Maeda. Appl. Phys. Lett. **106**, *2*, 022109 (2015).
[100] H. Dezaki, M.L. Jing, S. Balasekaran, T. Tanabe, Y. Oyama. Key Eng. Mater. **500**, 66 (2012).

[101] A.V. Andrianov, A.O. Zakhar'in, R.Kh. Zhukavin, V.N. Shastin, N.V. Abrosimov, A.V. Bobylev. JETP Lett. **100**, *12*, 771 (2014).
[102] D.A. Firsov, L.E. Vorobjev, V.Yu. Panevin, A.N. Sofronov, R.M. Balagula, I.S. Makhov, D.V. Kozlov, A.P. Vasil'ev. Semicond. **49**, *1*, 28 (2015).
[103] I.S. Makhov, V.Yu. Panevin, D.A. Firsov, L.E. Vorobjev, A.P. Vasil'ev, N.A. Maleev. J. Lumin. **210**, 352 (2019).
[104] I.S. Makhov, V.Yu. Panevin, D.A. Firsov, L.E. Vorobjev, G.V. Klimko. J. Appl. Phys. **126**, *17*, 175702 (2019).
[105] E.W. Williams, H.B. Bebb. In: Semiconductors and Semimetals. V. 8 / Eds R.K. Willardson, A.C. Beer. Academ. Press, N.Y., London (1972). P. 321.
[106] A.A. Berg, P.J. Dean. Light-Emitting Diodes. Clarendon Press, Oxford (1976). 591 p.
[107] A.O. Zakhar'in, A.V. Andrianov, A.G. Petrov, N.V. Abrosimov, R.Kh. Zhukavin, V.N. Shastin. Mater. Sci. Eng. B **286**, 115979 (2022).
[108] A.V. Andrianov, A.O. Zakhar'in. Phys. Status Solidi B **256**, *6*, 1800496 (2019).
[109] A.V. Andrianov, A.O. Zakhar'in, A.G. Petrov. Mater. Sci. Eng. B **263**, 114892 (2021).
[110] A.V. Andrianov, A.O. Zakhar'in. Appl. Phys. Lett. **112**, *4*, 041101 (2018).
[111] A.V. Andrianov, J.P. Gupta, J. Kolodzey, V.I. Sankin, A.O. Zakhar'in, Yu.B. Vasil'ev. Appl. Phys. Lett. **103**, *22*, 221101 (2013).
[112] P.G. Glasow, G. Ziegler, W. Suttrop, G. Pensl, R. Helbig. Proceed. SPIE **866**, 40 (1988).
[113] G. Ivanov, B. Magnusson, E. Janzen. Phys. Rev. B **67**, *16*, 165212 (2003).
[114] W. Gotz, A. Schoner, G. Pens1, W. Suttrop, W.J. Choyke. J. Appl. Phys. **73**, *7*, 3332 (1993).
[115] Q. Chen, J. Zeman, F. Engelbrecht, C. Peppemuller, R. Helbig, J.H. Chen, G. Martinez. J. Appl. Phys. **87**, *8*, 3800 (2000).
[116] C.Q. Chen, R. Helbig, F. Engelbrecht, J. Zeman. Appl. Phys. A **72**, *6*, 717 (2001).
[117] S.R. Smith, A.O. Evwaraye, W.C. Mitchel, M.A. Capano. J. Electron. Mater. **28**, *3*, 190 (1999).
[118] A.O. Zakhar'in, Yu.B. Vasilyev, N.A. Sobolev, V.V. Zabrodskii, S.V. Egorov, A.V. Andrianov. Semicond. **51**, *5*, 604 (2017).
[119] V.N. Abakumov, P.I. Perel', I.N. Yassievich. JETP **51**, *3*, 626 (1980).
[120] T. Timusk, H. Navarro, N.O. Lipari, M. Altarelli. Solid State Commun. **25**, *4*, 217 (1978).
[121] N.O. Lipari, A. Baldereschi. Phys. Rev. B **3**, *8*, 2497 (1971).
[122] T.M. Rice, J.C. Hensel, T.G. Phillips, G.A. Thomas. The Electron–Hole Liquid in Semiconductors. Academ. Press Inc., N.Y. (1977). 349 p.
[123] A.V. Andrianov, A.O. Zakhar'in, A.G. Petrov. JETP Lett. **109**, *12*, 781 (2019).
[124] M. Kira, S.W. Koch. Phys. Rev. Lett. **93**, *7*, 076402 (2004).
[125] G.K. Vlasov, S.G. Kalenkov. Int. J. Infrared Millimeter Waves **4**, *6*, 955 (1983).
[126] R. Huber, B.A. Schmid, Y.R. Shen, D.S. Chemla, R.A. Kaindl. Phys. Rev. Lett. **96**, *1*, 017402 (2006).
[127] P.I. Khadzhi, I.V. Belousov, A.V. Korovai, D.A. Markov. Tech. Phys. Lett. **38**, *6*, 261 (2012).
[128] R.G. Carter. Electromagnetic Waves: Microwave Components and Devices. Chapman & Hall, London (1990). 331 p.
[129] R.M. Weikle, T.W. Crowe, E.L. Kollberg. Int. J. Hi. Speed Electron. Syst. **13**, *2*, 429 (2003).
[130] V.A. Anfertiev, V.L. Vaks, I.V. Pentin, G.N. Goltsman, S.V. Seliverstov, M.I. Finkel, S.A. Ryabchun, I.V. Tretyakov. Radiofizika. Vestn. Nizhegorodskogo un-ta im. N.I. Lobachevskogo, *P. 1. 2*, 126 (2014). (in Russian).
[131] D.G. Pavel'ev, N.V. Demarina, Yu.I. Koshurinov, A P. Vasil'ev, E.S. Semenova, A.E. Zhukov, V.M. Ustinov. Semicond. **38**, *9*, 1105 (2004).
[132] D.G. Paveliev, Y.I. Koshurinov, A.S. Ivanov, A.N. Panin, V.L. Vax, V.I. Gavrilenko, A.V. Antonov, V.M. Ustinov, A.E. Zhukov. Semicond. **46**, *1*, 121 (2012).
[133] R. Sekiguchi, Y. Koyama, T. Quchi. Appl. Phys. Lett. **96**, *6*, 062115 (2010).
[134] M. Asada, S. Suzuki. Sensors **21**, *4*, 1384 (2021).
[135] T. Maekawa, H. Kayama, S. Suzuki, M. Asada. Appl. Phys. Express **9**, *2*, 024101 (2016).
[136] R. Isumi, S. Suzuki, M. Asada. Proc. of 42nd Int. Conf. IR, MM, THz waves. Cancun, Mexico, 27 August–1 September (2017). Contribution No. MA3.1.
[137] M. Asada, S. Suzuki, T. Fukuma. AIP Adv. **7**, *11*, 115226 (2017).
[138] K. Karashima, R. Yokoyama, M. Shiraishi, S. Suzuki, A. Aoki, M. Asada. Jpn. J. Appl. Phys. **49**, *2R*, 020208 (2010).
[139] K. Ogino, S. Suzuki, M. Asada. J. Infrared Millim. Terahertz Waves **38**, *12*, 1477 (2017).
[140] S. Kitagawa, K. Ogino, S. Suzuki, M. Asada. Jpn. J. Appl. Phys. **56**, *4*, 040301 (2017).
[141] M. Bezhko, S. Suzuki, M. Asada. Jpn. J. Appl. Phys. **59**, *3*, 032004 (2020).
[142] S. Kitagawa, S. Suzuki, M. Asada. Electron. Lett. **52**, 479 (2016).
[143] S. Kitagawa, M. Muzuno, S. Saito, K. Ogino, S. Suzuki, M. Asada. Jpn. J. Appl. Phys. **56**, *5*, 058002 (2017).
[144] S. Kasagi, S. Suzuki, M. Asada. J. Appl. Phys. **125**, *15*, 151601 (2019).
[145] S. Suzuki, M. Shiraishi, H. Shibayama, M. Asada. IEEE J. Sel. Top. Quantum Electron. **19**, *1*, 8500108 (2013).
[146] K. Miyamoto, A. Yamaguchi, T. Mukai. Jpn. J. Appl. Phys. **55**, *3*, 032201 (2016).
[147] K. Okamoto, K. Tsurida, S. Diebold, S. Hisatake, M. Fujita, T. Nagatsuma. J. Infrared Millim. Terahertz Waves **38**, *9*, 1085 (2017).
[148] N. Oshima, K. Hashimoto, S. Suzuki, M. Asada. IEEE Trans. Terahertz Sci. Technol. **7**, *5*, 593 (2017).
[149] V. Radisic, X.B. Mei, W.R. Deal, W. Yoshida, P.H. Liu, J. Ueda, M. Barsky, L. Samoska, A. Fug, T. Gaier, R. Lai. IEEE Microwave. Wireless Comp. Lett. **17**, *3*, 223 (2007).
[150] Y.M. Tousi, O. Momeni, E. Afshari. IEEE J. Solid State Circuits **47**, *12*, 3032 (2012).
[151] U.R. Pfeiffer, Y. Zao, J. Grzyb, R.A. Hadi, N. Sarmah, W. Förster, H. Rücker, B. Heinemann. IEEE J. Solid State Circuits **49**, *12*, 2938 (2014).
[152] Z. Hu, M. Mehmet, R. Han. IEEE J. Solid State Circuits **53**, *5*, 1313 (2018).
[153] R.L. Schmid, A.Ç. Ulusoy, S. Zeinolabedinzadeh, J.D. Cressler. IEEE Trans. Electron Devices **62**, *6*, 1803 (2015).
[154] M. Urteaga, R. Pierson, P. Rowell, V. Jain, E. Lobisser, M.J.W. Rodwell. Proc. 69th Annu. Device Res. Conf. Santa Barbara, CA, USA (2011). P. 281–282.

[155] M. Seo, M. Urteaga, J. Hacker, A. Young, Z. Griffith, V. Jain, R. Pierson, P. Rowell, A. Skalare, A. Peralta, R. Liu, D. Pukala, M. Rodwell. IEEE J. Solid State Circuits **46**, *10*, 2203 (2011).
[156] M. Urteaga, Z. Griffith, M. Seo, J. Hacker, M.J.W. Rodwell. Proc. IEEE **105**, *6*, 1051 (2017).
[157] U.A. Abdullin, G.A. Lyakhov, O.V. Rudenko, A.S. Chirkin. JETP **39**, *4*, 633 (1974).
[158] D.H. Auston, K.P. Cheung, J.A. Valdmanis, D.A. Kleinman. Phys. Rev. Lett. **53**, *16*, 1555 (1984).
[159] D.H. Auston, K.P. Cheung, P.R. Smith. Appl. Phys. Lett. **45**, *3*, 284 (1984).
[160] V.L. Malevich, P.A. Ziaziukia, R. Norkus, V. Pacebutas, I. Nevinskas, A. Krotkus. Sensors **21**, *12*, 4067 (2021).
[161] Y.-S. Lee. Principles of Terahertz Science and Technology. Springer Science + Business Media LLC (2009). 340 p.
[162] A.V. Andrianov, A.N. Aleshin, V.N. Truhin, A.V. Bobylev. J. Phys. D **44**, *26*, 265101 (2011).
[163] T.-I. Jeon, D. Grischkowsky, A.K. Mukherjee, R. Menon. Appl. Phys. Lett. **77**, *16*, 2452 (2000).
[164] J. Neu, C.A. Schmuttenmaer. J. Appl. Phys. **124**, *23*, 231101 (2018).
[165] Z. Liliental-Weber, H.J. Cheng, S. Gupta, J. Whitaker, K. Nichols, F.W. Smith. J. Electron. Mater. **22**, *12*, 1465 (1993).
[166] E. Isgandarov, X. Ropagnol, M. Singh, T. Ozaki. Front. Optoelectron. **14**, *1*, 64 (2021).
[167] M. Tani, S. Matsuura, S. Sakai, S.-I. Nakashima. Appl. Opt. **36**, *30*, 7853 (1997).
[168] M. Tani, Y. Hiroda, C. Que, S. Tanaka, R. Hittori, M. Yamaguchi, S. Nishizawa. J. Infrared Millim. Terahertz Waves **27**, *4*, 531 (2006).
[169] Y. Cai, I. Brener, J. Lopata, J. Wynn, L. Pfeiffer, J. Federici. Appl. Phys. Lett. **71**, *15*, 2076 (1997).
[170] F. Miyamaru, Y. Saito, K. Yamamoto, T. Furuya, S. Nishizawa, M. Tani. Appl. Phys. Lett. **96**, *21*, 211104 (2010).
[171] M.V. Exter, D. Grischkowsky. IEEE Trans. Microwave Tech. **38**, *11*, 1684 (1990).
[172] S.E. Ralph, D. Grischkowsky. Appl. Phys. Lett. **60**, *9*, 1070 (1992).
[173] Y.C. Shen, P.C. Upadhya, H.E. Beere, E.H. Linfield, A.G. Davies, I.S. Gregory, C. Baker, W.R. Tribe, M.J. Evans. Appl. Phys. Lett. **85**, *2*, 164 (2004).
[174] R.B. Kohlhaas, S. Breuer, L. Liebermeister, S. Nellen, M. Deumer, M. Schell, M.P. Semtsiv, W.T. Masselink, B. Globisch. Appl. Phys. Lett. **117**, *13*, 131105 (2020).
[175] J.T. Darrow, X.-C. Zhang, D.H. Auston. IEEE J. Quant. Electron. **28**, *6*, 1607 (1992).
[176] V.N. Trukhin, A.S. Buyskikh. Acta Phys. Polonica A **119**, *2*, 206 (2011).
[177] D. You, R.R. Jones, P.H. Bucksbaum, D.R. Dykaar. Opt. Lett. **18**, *4*, 290 (1993).
[178] A.E. Yachmenev, D.V. Lavrukhin, I.A. Glinskiy, N.V. Zenchenko, Y.G. Goncharov, I.E. Spector, R.A. Khabibullin, T. Osuji, D.S. Ponomarev. Optical Eng. **59**, *6*, 061608 (2019).
[179] https://www.batop.de/
[180] D.R. Bacon, T.B. Gill, M. Rosamond, A.D. Burnett, A. Dunn, L. Li, E.H. Linfield, A.G. Davies, P. Dean, J.R. Freeman. Opt. Express **28**, *12*, 17219 (2020).
[181] J. Madéo, N. Jukam, D. Oustinov, M. Rosticher, R. Rungsawang, J. Tignon, S.S. Dhillon. Electron. Lett. **46**, *9*, 611 (2010).
[182] N.T. Yardimci, S.-H. Yang, C.W. Berry, M. Jarrahi. IEEE Trans. Terahertz Sci. Technol. **5**, *2*, 223 (2015).
[183] S.-H. Yang, M.R. Hashemi, C.W. Berry, M. Jarrahi. IEEE Trans. Terahertz Sci. Technol. **4**, *5*, 575 (2014).
[184] X.-C. Zhang, D. Auston. J. Appl. Phys. **71**, *1*, 326 (1992).
[185] S.L. Chuang, S. Schmitt-Rink, B.I. Greene, P.N. Saeta, A.F.J. Levi. Phys. Rev. Lett. **68**, *1*, 102 (1992).
[186] A. Rice, Y. Jin, X. Ma, X.-C. Zhang, D. Bliss, J. Larkin, M. Alexander. Appl. Phys. Lett. **64**, *11*, 1324 (1994).
[187] A. Bonvalet, M. Joffre, J.L. Martin, A. Migus. Appl. Phys. Lett. **67**, *20*, 2907 (1995).
[188] R. Kaindl, D. Smith, M. Joschko, M. Hasselbeck, M. Woerner, T. Elsaesser. Opt. Lett. **23**, *11*, 861 (1998).
[189] P.Y. Han, X.-C. Zhang. Appl. Phys. Lett. **73**, *21*, 3049 (1998).
[190] Q. Wu, X.-C. Zhang. Appl. Phys. Lett. **71**, *10*, 1285 (1997).
[191] R. Kaindl, F. Eickemeyer, M. Woerner, T. Elsaesser. Appl. Phys. Lett. **75**, *8*, 1060 (1999).
[192] X.-C. Zhang, B.B. Hu, J.T. Darrow, D.H. Auston. Appl. Phys. Lett. **56**, *11*, 1011 (1990).
[193] X.-C. Zhang, J.T. Darrow, B.B. Hu, D.H. Auston, M.T. Schmidt, P. Tham, E.S. Yang. Appl. Phys. Lett. **56**, *22*, 2228 (1990).
[194] X.-C. Zhang, B.B. Hu, S.H. Xin, D.H. Auston. Appl. Phys. Lett. **57**, *8*, 753 (1990).
[195] X.-C. Zhang, Y. Jin, K. Yang, L.J. Schowalter. Phys. Rev. Lett. **69**, *15*, 2303 (1992).
[196] X.-C. Zhang, Y. Jin, T.D. Hewitt, T. Sangdiri, L.E. Kingsley, W. Weiner. Appl. Phys. Lett. **62**, *17*, 2003 (1993).
[197] M. Li, F.G. Sun, G.A. Wagoner, M. Alexander, X.-C. Zhang. Appl. Phys. Lett. **67**, *1*, 25 (1995).
[198] S.C. Howells, L.A. Schlie. Appl. Phys. Lett. **67**, *25*, 3688 (1995).
[199] N. Sarukura, H. Ohtake, S. Izumida, Z. Liu. J. Appl. Phys. **84**, *1*, 654 (1998).
[200] P. Gu, M. Tani, S. Kono, K. Sakai, X.-C. Zhang. J. Appl. Phys. **91**, *9*, 5533 (2002).
[201] K. Liu, J. Xu, T. Yuan, X.-C. Zhang. Phys. Rev. B **73**, *15*, 155330 (2006).
[202] C. Song, P. Wang, Y. Qian, G. Zhou, R. Nötzel. Opt. Express **28**, *18*, 25750 (2020).
[203] V.N. Trukhin, V.A. Solov'ev, I.A. Mustafin, M.Yu. Chernov. Tech. Phys. Lett. **48**, *2*, 42 (2022).
[204] K. Seeger. Semiconductor Physics. Springer-Verlag, Wien (1973).
[205] R. Adomavičius, A. Urbanowicz, G. Molis, A. Krotkus, E. Šatkovskis. Appl. Phys. Lett. **85**, *13*, 2463 (2004).
[206] J.F. Ward, J.K. Guha. Appl. Phys. Lett. **30**, *6*, 276 (1977).
[207] M.B. Johnston, D. Whittaker, A. Corchia, A.G. Davies, E.H. Linfield. Phys. Rev. B **65**, *16*, 165301 (2002).
[208] S. Howells, S. Herrera, L. Schlie. Appl. Phys. Lett. **65**, *23*, 2946 (1994).
[209] L. Xu, X.-C. Zhang, D.H. Auston, B. Jalali. Appl. Phys. Lett. **59**, *26*, 3357 (1991).
[210] A.V. Andrianov, A.N. Aleshin, S.N. Abolmasov, E.I. Terukov, E.V. Beregulin. JETP Lett. **116**, *12*, 859 (2022).
[211] A.V. Andrianov, A.N. Aleshin, S.N. Abolmasov, E.I. Terukov, A.O. Zakhar'in. Phys. Solid State **65**, *5*, 814 (2023).
[212] A.S. Abramov, D.A. Andronikov, S.N. Abolmasov, E.I. Terukov. In: High-Efficient Low-Cost Photovoltaics / Eds V. Petrova-Koch, R. Hezel, A. Goetzberger. Springer Nature Switzerland AG, Cham (2020). Ch. 7. P. 113–132.

[213] Y. Kadoya, T. Matsui, A. Takazato, J. Kitagawa. Joint Proceed. 32nd Int. Conf. on Infrared and Millimeter Waves and the 15th Int. Conf. Terahertz Electronics, 02-09 September. Cardiff, UK (2007). P. 987–988.
[214] A. Lisauskas, A. Reklaitis, R. Venckevičius, I. Kašalynas, G. Valušis, G. Grigaliūnaitė-Vonsevičienė, H. Maestre, J. Schmidt, V. Blank, M.D. Thomson, H.G. Roskos, K. Köhler. Appl. Phys. Lett. **98**, *9*, 091103 (2011).
[215] A. Reklaitis. Phys. Rev. B **77**, *15*, 153309 (2008).
[216] H.G. Roskos, M.C. Nuss, J. Shah, K. Leo, D.A. Miller, A.M. Fox, S. Schmitt-Rink, K. Köhler. Phys. Rev. Lett. **68**, *14*, 2216 (1992).
[217] P.C.M. Planken, M.C. Nuss, I. Brener, K.W. Goossen, M.S.C. Luo, S.L. Chuang, L. Pfeifer. Phys. Rev. Lett. **69**, *26*, 3800 (1992).
[218] S. Bell, J. Rogers, J.N. Heyman, J.D. Zimmerman, A.C. Gossard. Appl. Phys. Lett. **92**, *14*, 142108 (2008).
[219] P.C.M. Planken, M.C. Nuss, W.H. Knox, D.A.B. Miller, K.W. Goossen. Appl. Phys. Lett. **61**, *17*, 2009 (1992).
[220] A.V. Andrianov, P.S. Alekseev, G.V. Klimko, S.V. Ivanov, V.L. Shcheglov, M.A. Sedova, A.O. Zakhar'in. Semicond. **47**, *11*, 1433 (2013).
[221] A.V. Andrianov, P.S. Alekseev, G.V. Klimko, S.V. Ivanov, V.L. Sheglov, I.V. Sedova, A.O. Zakhar'in. Semicond. Sci. Technol, **28**, 105012 (2013).
[222] C. Washke, H.G. Roskos, R. Schwedler, K. Leo, H. Kurtz, K. Köhler. Phys. Rev. Lett. **70**, *21*, 3319 (1993).
[223] F. Bloch. Z. Phys. **52**, 555 (1928).
[224] C. Zener. Proc. R. Soc. London Ser. A **145**, *855*, 523 (1934).
[225] G.N. Wannier. Phys. Rev. **117**, *2*, 432 (1960).
[226] P. Voisin. Ann. Phys. **22**, *6*, 681 (1997).
[227] J. Bleuse, G. Bastard, P. Voisin. Phys. Rev. Lett.**60**, *3*, 220 (1988).
[228] Y. Shimada, K. Hirokawa, M. Odnoblioudov, K.A. Chao. Phys. Rev. Lett. **90**, *4*, 046806 (2003).
[229] V.I. Sankin, A.V. Andrianov, A.O. Zakhar'in, A.G. Petrov. JETP Lett. **94**, *5*, 362 (2011).
[230] V.I. Sankin, A.V. Andrianov, A.O. Zakhar'in, A.G. Petrov. Appl. Phys. Lett. **100**, *11*, 111109 (2012).
[231] V.I. Sankin. Semicond. **36**, *7*, 717 (2002).
[232] L.S. Ramsdell. Amer. Mineral. **32**, *1–2*, 64 (1947).
[233] V.A. Maksimenko, V.V. Makarov, A.A. Koronovskii, A.E. Hramov, R. Venckevičius, G. Valušis, A.G. Balanov, F.V. Kusmartsev, K.N. Alekseev. JETP Lett. **103**, *7*, 465 (2016).
[234] V.I. Sankin, A.V. Andrianov, A.G. Petrov, A.O. Zakhar'in. Appl. Phys. Lett. **108**, *21*, 211108 (2016).
[235] E.R. Brown. Proc. SPIE **7938**, 793802 (2011).
[236] R. Safian, G. Ghazi, N. Mohammadian. Opt. Eng. **58**, *11*, 110901 (2019).

Translated by I.Mazurov